University of Naples Federico II

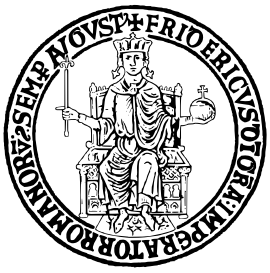

Polytechnic School and Basic Sciences

Department of Physical Sciences and Technologies

Master's Degree Course in Physics of Matter

Electromagnetic properties of hybrid Josephson junctions

Relatori
Prof. Francesco Tafuri
Dr. Domenico Montemurro

Correlatore
Prof. Giovanni Ausanio

Candidato
Marcello Pio Guardascione
N94000708

Anno Accademico 2022–2023

University of Naples Federico II

Polytechnic School and Basic Sciences

Department of Physical Sciences and Technologies

Master's Degree Course in Physics of Matter

Electromagnetic properties of hybrid Josephson junctions

Relatori
Prof. Francesco Tafuri
Dr. Domenico Montemurro

Correlatore
Prof. Giovanni Ausanio

Candidato
Marcello Pio Guardascione
N94000708

Anno Accademico 2022–2023

Contents

Introduction

In the realm of quantum technology, the quest for superconducting quantum bits (qubits) has fueled a continuous drive for innovation in the fabrication and characterization of Josephson junctions (JJs), which are the key elements for all superconducting qubits. Among these JJs, those crafted from Aluminum technology have emerged as the fundamental building blocks for superconducting quantum circuits. This has not prevented the search of alternative solutions especially in the direction of flexible components that could favor hybrid systems. For example, Josephson junctions employing ferromagnetic barriers offer unique properties [1], which are of interest for a variety of applications ranging from novel types of superconducting qubits to spintronics.

Progresses in the realization of high-quality ferromagnetic Josephson junctions, primarily relying on aluminum technology, represents a significant stride in the advancement of quantum circuitry. In analogy with Niobium-based technology, we have embraced an innovative fabrication process to attain very high-quality hybrid Aluminum Josephson junctions [2].

In this thesis a comparative study on ferromagnetic JJs using both Nb and Al as superconducting electrodes, and $Ni_{80}Fe_{20}$ as barrier, is carried out. These junctions incorporate robust ferromagnetic inter-layers, such as the $Ni_{80}Fe_{20}$ alloy, often referred to as Permalloy [3]. Such alloys hold the promise of realizing memory elements characterized by reduced footprint and high characteristic voltage, leading them to become viable candidates for applications in random access memories (RAM). Moreover, these innovations extend their utility to the domain of quantum computing, where these devices can be integrated in superconducting quantum circuits possibly displaying quite unique properties.

We will therefore describe the fabrication process and presenting the main DC transport properties of the junctions employing the ferromagnetic alloy (SFS) and those based on TaS_2 van der Waals material, including their current-voltage characteristics, critical current as a function of temperature, and responses to external magnetic fields. Van der Waals based structures are strongly related to the SFS JJs since recently [1] has been shown how combining van der Waals ferromagnet and spin-singlet superconductors it is possible to investigate a set of fundamental phenomenon like to induce pair correlations at superconductor/ferromagnet interfaces, or the supercurrent over much longer distances in the barrier and built innovative 2D superconducting devices that may find application in the field of the spintronics.

This thesis is structured as follows:

- Chapter 1: The physics of the Josephson effect is introduced with a special focus on the theories useful to support the magneto-transport measurements.
- Chapter 2: It introduces the used cryogenic (dilution refrigerator) and measurement set-up. We discuss the role of filters and the techniques involved in controlling the temperature within the cryostat. Moreover, various measurement techniques, such as current-voltage measures, magnetic field-dependent measurements, and conductance-voltage measurements, will be shown.
- Chapter 3: Here, we delve into the developed process of useful for building the studied devices used.
- Chapter 4: We turn our attention on the transport measurements of the SIS (Superconductor-Insulator-Superconductor) and SIs'FS (Superconductor-Insulator-Superconductor-Ferromagnet-Superconductor) Josephson junctions based on Aluminum and Niobium, investigating their transport properties and relevance in our research.
- Chapter 5: As we delve into the latter part of this thesis, we shift our focus on another type of hybrid Josephson junctions based on 1T-TaS_2, a Van der Waals material [4]. Specifically, our research aims at inducing superconductivity in thin flakes of 1T-TaS_2 by proximity effect, a project which is still under development.

–1–
Theory of Superconductivity

1.1 Basic Superconductivity

1.1.1 Brief History of Superconductivity

In 1911 Kamerlingh Onnes discovered a new state of matter, which we now call "Superconductivity" [5]. In studying the electrical resistance of mercury at low temperature, Onnes observed that, at about $4.2K$, the electrical resistance of a chip made of sharply dropped by several orders of magnitude, reaching absolute zero.

What really characterizes the superconducting phase is not only the absence of resistance to the current flow, but also the perfect expulsion of magnetic fields from the bulk material. It is due to the presence of screening currents that are generated in the outermost layer of the superconductor. It was 1933 when Walther Meissner and Robert Ochsenfeld discovered that superconductors expelled applied magnetic fields, a phenomenon that has come to be known as the Meissener Effect [6]. Complete expulsion occurs up to a maximum value of the external magnetic field, as reported in Table 1.1.

In 1935, brothers Fritz London and Heinz London proved using a phenomenological model that the Meissner effect was a consequence of the minimization of the electromagnetic free energy carried by superconducting current [7]. In 1950, a first phenomenological Ginzburg–Landau theory that allows an interpretation of the superconductive properties of the matter was devised by Lev Landau and Vitaly Ginzburg [8].

The Ginzburg–Landau theory, which combined Landau's theory of second-order phase transitions with a Schrödinger-like wave equation, had great success in explaining the macroscopic properties of superconductors. In particular, Alexei Abrikosov showed that Ginzburg–Landau theory predicts the division of superconductors into the two categories now referred to as Type I and Type II. Abrikosov and Ginzburg were awarded the 2003 Nobel Prize in Physics for their work [9]. Also in 1950, Emanuel Maxwell [10] and, almost simultaneously, C.A. Reynolds et al. [11] found that the critical temperature of a superconductor depends on the isotopic mass of the constituent elements . This important discovery pointed to the electron-phonon interaction as the microscopic mechanism responsible for superconductivity.

The complete microscopic theory of superconductivity was finally proposed in 1957 by John Bardeen, Leon N. Cooper, and Robert Schrieffer (BCS) [12]. It was the former theory that modelled the superconducting current as a super-fluid of Cooper pairs, i.e. pairs of electrons interacting through the exchange of phonons. For this work, the authors were awarded the Nobel Prize in Physics in 1972. Brian Josephson was awarded the Nobel

Superconductor	$T_C(K)$	H_C**(0) (T)**
Al	1.17	0.01
Sn	3.72	0.03
Pb	7.19	0.08
Hg	4.15	0.04
Nb	9.25	0.2
V	5.40	0.14
V_3Ga	16.5	27
V_3Si	17.1	25
Nb_3Al	20.3	34
Nb_3Ge	23.3	38
MgB_2	40	≈ 5; ≈ 20
Rb_2CsC_{60}(fullerene)	31.3	≈ 30
$NdFeAsO_{0.7}F_{0.3}$(iron pnictide)	47	≈ 30; ≈ 50
$La_{2-x}Sr_xCuO_4$ (x ≈ 0.15)	38	≈ 45
$YBa_2Cu_3O_7$	92	≈ 140
$Bi_2Sr_2CaCu_2O_8$	89	≈ 107
$Tl_2Ba_2Ca_2Cu_3O_{10}$	125	≈ 75

Table 1.1: The modified table includes the data from [13]. T_c and H_c represents, the critical current and the magnetic field that leads to a full phase transition to the normal state (H_c) of the materials. (H_{c1} for elements, while H_{c2} for the others.

Prize in Physics for his important theoretical prediction that a super-current can flow between two pieces of superconductor separated by a thin layer of insulator [14]. This phenomenon, called the Josephson effect, is exploited by superconducting devices such as SQUIDs.

Since 1911, superconductivity has been found in several elements and in more than one thousand alloys. The element with the highest transition temperature is Niobium with $T_c = 9.25K$. In 1973 Nb_3Ge found to have T_c of $23K$, which remained the highest ambient-pressure T_c until the discovery of the cuprate high-temperature superconductors in 1986. The run to the achievement of materials with the highest critical temperature has been sharply accelerated after the discovery by Bednorz and Müller of the superconducting properties of La-based cuprates, with T_c in excess of $30K$ [15]. Soon, other families of superconducting cuprate oxides were discovered, and the achievements of materials with critical temperatures above $77K$ (the boiling point of liquid nitrogen) passed suddenly from dream to reality. Recently other types of superconductivity have been discovered,

such as Iron-pnictides and fullerene, and it's superconducting parameters are summarized in the table 1.1 taken from [13].

1.1.2 London Theory

F. and H. London (1935) developed a model useful to interpreted the properties shown by a superconducting material. The model takes into account an ordinary conductor with n electrons per unit volume with effective mass m where the electrons moving in the material can be scattered by impurities, phonons, and other defects. Assuming for simplicity that the carrier dynamics can be characterized with some finite relaxation time τ, the average drift velocity of the carriers in the presence of an electric field is $\vec{v}_d = -e\tau\vec{E}$, and the current density is given by the Ohm law $\vec{J} = \sigma\vec{E}$ with $\sigma = \frac{2ne\tau}{m}$.

Let's consider now an ideally pure metal, with a parabolic conduction band, and n electrons per unit volume of effective mass m. In the presence of an electric field E, the motion of each freely moving electron is described by the ballistic dynamic equation:

$$m\frac{d\vec{v}}{dt} = -e\vec{E}. \tag{1.1}$$

By considering the current density $\vec{J} = -ne\vec{v}$, we can derive **first London's equation**:

$$\frac{\partial\vec{J}}{\partial t} = \frac{ne^2}{m}\vec{E}. \tag{1.2}$$

It suggests that when the magnetic field changes over time $\frac{\partial B}{\partial t} \neq 0$, a corresponding current density is induced to counteract the change. This effect refers to the property of excluding fields and currents from its interior. By applying the procedure describe in [16] we can derive the **second London's equation** :

$$\nabla \times \vec{J} = -\frac{n_s e^2}{mc}\vec{B} \tag{1.3}$$

In the case of steady-state conditions, the relationship between the magnetic field and the current density allows to obtain:

$$\nabla^2\vec{B}(\vec{r}) = \frac{1}{\lambda_L^2}\vec{B}(\vec{r})$$

thus allowing to define the London penetration length λ_L , which is given by:

$$\lambda_L = \frac{c}{\omega_p} = \sqrt{\frac{mc^2}{4\pi n_s e^2}} \tag{1.4}$$

Here, ω_p represents the plasma frequency corresponding to the electron density n_s. For electron concentrations typical of metals, the length λ_L is on the order of $\approx 10^2$ Å (as seen in Table 1.2), assuming that all electrons behave ballistically ($n = n_s$).

Material	ξ_0 (nm)	λ_L (nm)	λ_L/ξ_0	$\Delta_0(meV)$
Sn	230	34	0.16	0.56
Al	1600	16	0.010	0.182
Pb	83	37	0.45	1.1
Nb	38	39	1.02	1.4

Table 1.2: Coherence length ξ_0, London penetration depth λ_L and superconducting gap Δ_0 for various materials [17].

1.1.3 The Microscopic Theory

The Bardeen Cooper Schriffer (BCS) theory of superconductivity is a mean-field theory [13, 16] that describes the attractive interaction of two electrons placed on the Fermi surfaces by the exchange of a phonon. The BCS theory is a microscopic theory that derived from several significant theoretical predictions, independently of the specific details of the interaction. These quantitative predictions, as outlined below, remain valid for any sufficiently weak attraction between electrons[13].

The first prediction of the BCS theory is the Cooper pair formation: electrons are bound into Cooper pairs, and these pairs are correlated due to the Pauli exclusion principle for the electrons, from which they are constructed. Therefore, breaking a pair requires changing the energies of all other pairs [16]. This implies the existence of an energy gap for single-particle excitation, unlike in a normal metal, where the state of an electron can be changed by adding an arbitrarily small amount of energy. This energy gap is highest at low temperatures but vanishes at the transition temperature, commonly referred as T_c (critical temperature), when superconductivity ceases to exist. The energy gap is most directly observed in tunneling experiments and in the reflection of microwaves from superconductors.

The superconducting gap is strictly related to the **coherence length** ξ_0 at $T = 0$ of the copper pairs according to the following relation [16]:

$$\xi_0 = \frac{\hbar v_F}{\pi \Delta} \tag{1.5}$$

Numerical examples of coherence lengths and superconducting gaps for some materials can be found in table 1.2.

BCS theory also predicts the relationship between **energy gap** Δ and the temperature T. The energy gap's value at zero temperature is related to the critical temperature (in energy units) by the universal value: $\Delta(T = 0) = 1.764 k_B T_c$ which is independent of the material. Near the critical temperature, the relationship approaches: $\Delta(T \to T_c) \approx 3.06 k_B T_c \sqrt{1 - (T/T_c)}$, as show in Fig. 1.1. An interpolation formula that comes from the BCS for $\Delta(T)$, which respect either the $T \to 0$ and the $T \to T_c$ behaviour is [18]:

$$\Delta(T) = \Delta_0 \tanh\left(1.74\sqrt{\frac{T_c}{T} - 1}\right) \tag{1.6}$$

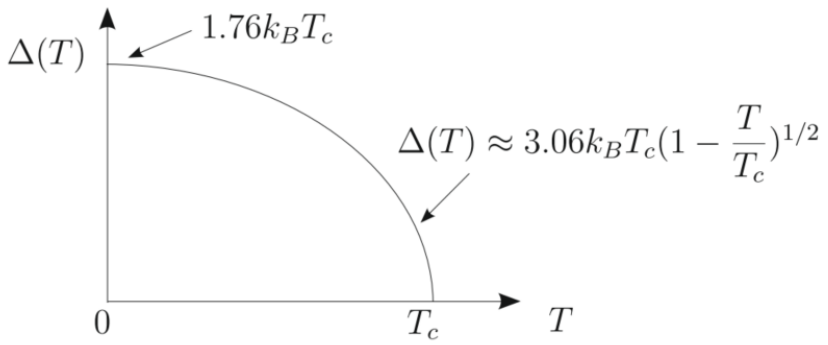

Figure 1.1: Trend of the superconducting gap as a function of temperature for a superconductor of pure material [13]. Both limits, for $T \longrightarrow 0$ and $T \longrightarrow T_c$, are shown.

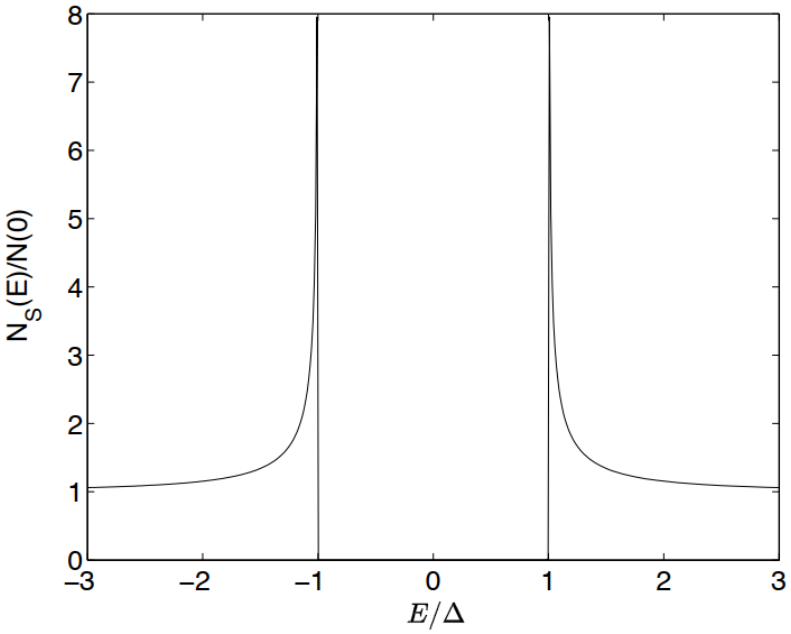

Figure 1.2: Superconducting density of states [13].

BCS also describes how the **density of states** $N(E)$ changes when a material enters in the superconducting state, where there are no electronic states at the Fermi level. The density of states for quasi-particle excitations, excitations of the superconducting ground state, can be described by the expression (see [19]):

$$N_S(E) = N_F \frac{|E|}{\sqrt{E^2 - |\Delta^2|}} \theta(|E| - |\Delta|) \tag{1.7}$$

Here, E is measured relative to the Fermi level E_F, and N_F represents the density of states at $E = E_F$ when the sample is in the normal state. This function is depicted in Fig. 1.2.

The Eq. 1.7 exhibits two main features that are observed in superconducting experiments. Firstly, there is the energy gap $|\Delta|$: for $|E| < |\Delta|$, there are no available states for the quasi-particles. Therefore, the pair potential is often referred to as the "gap function." Consequently, if the temperature is much lower than $|\Delta|$, the behavior of the superconductor is unaffected by quasi-particles. The second significant feature is the BCS divergence of the density of states at $E = |\Delta|$. However, for systems more complex then a bulk superconductor, states with energies within the gap can appear.

The density of the states is connected to the differential conductance, for example measurements made with STM can give an estimate of the density of the states precisely by calculating the variation of the electron current.

1.1.4 Ginzburg Landau Theory

The BCS microscopic theory of superconductivity provides valuable insights, but it presents significant challenges in terms of its formal and technical aspects. This is particularly evident when dealing with non-homogeneous systems that exhibit boundary effects, impurity effects, variations in Cooper pair density, magnetic fields, and other factors.

The Ginzburg-Landau phenomenological theory of second-order phase transitions proves to be a useful tool for this situations. This approach, which avoids the explicit use of many-body wavefunctions, employs a clever set of assumptions [8]. It draws upon the phenomenology of superconductors and incorporates certain insights from the microscopic theory. By doing so, it effectively describes and comprehends significant physical effects occurring near the normal metal-superconductor phase transition.

To explain the transition to the superconducting phase, Ginzburg and Landau introduce certain elements of their theory. They propose the use of a macroscopic complex function called the order parameter ψ, which represents the degree of ordering achieved when transitioning from the disordered phase ($T > Tc$) to the ordered phase ($T < Tc$) in the superconducting state. According to their theory, the complex order parameter $\psi(\vec{r})$ at a specific temperature T in the superconducting phase is directly linked to the local number of Cooper pairs by the equation $n_{pairs}(\vec{r}) = |\psi(\vec{r})|^2$ [16].

The fundamental assumption underlying the Ginzburg-Landau theory is that the free energy density of the superconductor can be expanded in a specific form near the

transition temperature [8, 20]. That is :

$$f_S(T,\psi,A) = f_N(T) + \alpha(T)|\psi|^2 + \frac{1}{2}\beta(T)|\psi|^4 + \frac{1}{2m^*}\left|\left(\vec{p} - \frac{e}{c}\vec{A}\right)\psi(\vec{r})\right|^2 + \frac{8B\pi^2}{2} \tag{1.8}$$

where $f_N(T)$ is the free energy density in the normal phase ($\psi = 0$), alpha and beta are two phenomenological parameters that we'll see below and the last term is the vacuum energy of the magnetic field. For a further description and a more physical derivation of the Eq 1.8 one can look at [20].

The two phenomenological quantities $\alpha(T)$ and $\beta(T)$ must satisfy 1.3:

T < Tc	**T > Tc**
$\beta(T) > 0$	$\beta(T) > 0$
$\alpha(T) < 0$	$\alpha(T) > 0$

Table 1.3: $\alpha(T)$ and $\beta(T)$ constraints in order to obtain the correct behaviour [13].

$$\alpha(T) = \alpha_0(T - T_c) \quad \text{and} \quad \beta(T) = \beta_0 \tag{1.9}$$

where $\alpha_0 > 0$ and $\beta_0 > 0$ for $T \approx T_c$. In fact, only with these constraints, the free energy change admits a negative minimum, at a finite value $|\psi|$, for $T \leq T_c$.

The total free energy in the volume V of the sample is then given by the space integral:

$$F_S(T) = \int_V f_S(T, \psi(\vec{r}), A(\vec{r}))\, d\vec{r} \tag{1.10}$$

The Ginzburg-Landau equation is obtained by minimizing the free energy $F_S(T)$ with respect to arbitrary variations of ψ^* or ψ. The variational calculation [20] reveals that the order parameter function ψ satisfies the **Ginzburg-Landau equation**.

$$\frac{1}{2m^*}\left(\vec{p} - \frac{e}{c}\vec{A}\right)^2 \psi(\vec{r}) + \beta|\psi(\vec{r})|^2\psi(\vec{r}) = -\alpha(T)\psi(\vec{r}) \tag{1.11}$$

The expression for the supercurrent density $\vec{J}_S(\vec{r})$ in terms of $\psi(\vec{r})$ can be written as:

$$\vec{J}_S(\mathbf{r}) = -\frac{i\hbar e^*}{2m^*}\left[\psi^*(\vec{r})\nabla\psi(\vec{r}) - \psi(\vec{r})\nabla\psi^*(\vec{r})\right] - \frac{e^{*2}}{m^*c}|\psi(\vec{r})|^2 A(\vec{r}) \tag{1.12}$$

Equation 1.12 takes on a particularly meaningful form when we express the complex macroscopic wavefunction in polar form as:

$$\psi(\vec{r}) = |\psi(\vec{r})|e^{i\theta(\vec{r})} \tag{1.13}$$

where $|\psi(\vec{r})|$ represents the modulus of the wavefunction and the real quantity $\theta(\vec{r})$ represents the phase. By substituting the above expression into the Ginzburg-Landau Eq. 1.11, the current density becomes:

$$\vec{J}(\vec{r}) = |\psi(\vec{r})|^2\left(-\frac{e^*\hbar}{m^*}\nabla\theta(\vec{r}) - \frac{e^{*^2}}{m^*c}\vec{A}(\vec{r})\right) \tag{1.14}$$

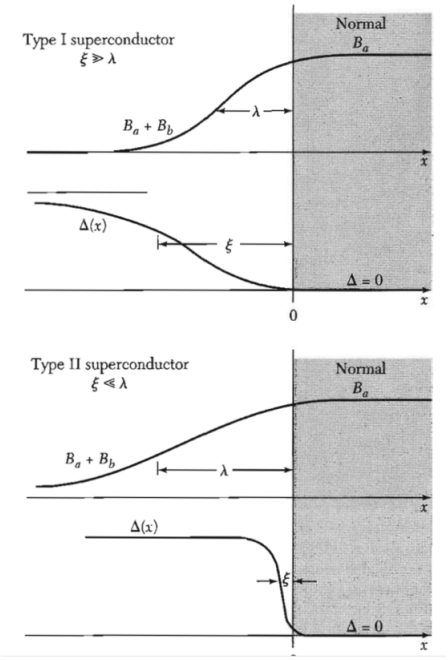

Figure 1.3: Magnetic coherence and penetration length for type I and II superconductors in the presence of a barrier between different materials. Both the trend of the magnetic field and that of the superconducting gap is represented [17].

The Ginzburg Landau Theory introduces two important quantities: the penetration length λ and the coherence length ξ. The penetration length tells you how deep magnetic fields can penetrate a superconductor, while the coherence length characterizes the size of the superconducting "islands" and is related to the size of vortices in a superconductor.

It's important to note that the Ginzburg-Landau theory provides approximate descriptions of these lengths, and in real materials, the values may be influenced by various factors. The theory is particularly useful for describing Type II superconductors and their transition between the Meissner state and the mixed state, where vortices (zone of normal material within the superconductor) and flux lines play a significant role.

The relationship between these two physical quantities is very important, introducing two types of superconductors as seen in Fig. 1.3.

1.1.5 Josephson Effect

The Josephson effect is a phenomenon observed in superconducting systems that exploits the phenomenon of quantum tunneling of Cooper pairs of electrons across a thin ($\approx nm$) insulating barrier between two superconductor. It was discovered by the British physicist Brian D. Josephson in 1962 and earned him the Nobel Prize in Physics in 1973. In order to understand the Josephson effect, let's consider a simplified model of a Josephson junction (Fig. 1.4). A Josephson junction (SIS) consists of two superconducting electrodes separated by a thin insulating barrier ($\approx nm$). The Josephson effect can be described by

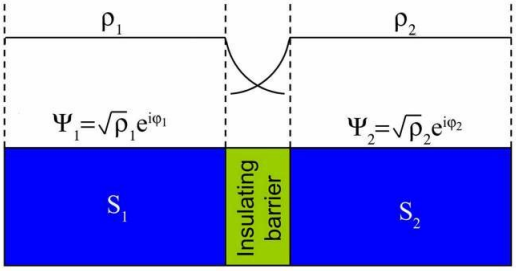

Figure 1.4: Qualitative appearance of the wave functions. The solutions must match smoothly at the edges of the tunneling barrier.

the Josephson relations, obtained in the appendix A , which relate the current flowing through the junction to the phase difference between the superconducting wave functions on either side of the Josephson junction.

$$\begin{cases} I = I_c sin(\phi), \\ \dfrac{d\phi}{dt} = \dfrac{2e}{\hbar} V. \end{cases} \tag{1.15}$$

The first one is the **Current-Phase Relationship**, it describes the relationship between the supercurrent flowing through the junction I and the phase difference across the junction ϕ. I_c represents the critical current of the junction. The critical current is the maximum current that can flow through the junction without any voltage drop across it, as seen in Fig. 1.5. This equation demonstrates that the super-current is a sinusoidal function of the phase difference. The second equation is called the **Voltage-Phase Relationship** and it relates the time derivative of the phase difference ($d\phi/dt$) to the voltage (V) across the junction. This equation illustrates that the time rate of change of the phase difference is proportional to the voltage applied across the junction.

One of the best ways to visualize the physics of Josephson's equations is by looking at the current-voltage characteristics of a SIS Josephson junction, depicted in Fig. 1.5. There are two components to the tunneling current flowing through the junction in Fig. 1.5. The first is from the tunneling of Cooper pairs. This super-current is described by the ac and dc Josephson relations 1.15. The second is the quasi-particle current, which, in the limit of zero temperature, arises when the energy from the bias voltage eV exceeds twice the value of superconducting energy gap Δ, then there is the switch from the super-current branch to the "normal" branch having a finite resistance R_n. At finite temperature, a small quasi-particle tunneling current - called the sub-gap current - is present even for voltages less than twice the energy gap due to the thermal promotion of quasi-particles above the gap, leading to the characteristics hysteresis behaviour of the I-V curve.

The product between the critical current and the normal resistance is an important parameter for a JJ. For the $I_c R_n$ product of a SIS junction follows the temperature trend know as the **Ambegaokar-Baratoff** relation [21]:

$$I_c R_n = \frac{\pi}{2} \frac{\Delta}{e} \tanh\left(\frac{\Delta}{2k_B T}\right) \tag{1.16}$$

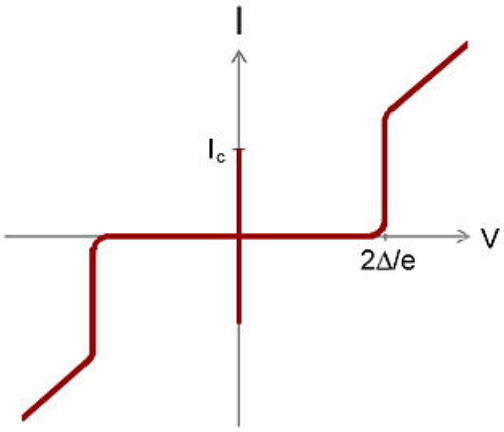

Figure 1.5: Current - Voltage Characteristic for a superconductor-insulator-superconductor tunnel junction.

Various models take into account the order of magnitude of I_cR_n and the concavity or convexity of its temperature trend [22]. To name a few AB, KO-1, KO-2 and ODSEE models whose theoretical trend is foreseen in the Fig 1.6.

1.1.6 Proximity Effect

Proximity effect describes how superconducting coherence is transferred from the S to a metallic, semiconducting or a ferromagnetic barrier, and obviously plays a significant role also in understanding the behavior of particles and JJs at the nanoscale.

In a SIS junction particles can pass through energy barriers that would be classically forbidden thanks to quantum tunneling. However, when the insulating barrier is replaced by a normal conductor, the physical phenomenon that allows transport at these junctions is different, and it's based on the Andreev reflections. The Andreev reflection is a fundamental process that occurs at the interface between a normal metal and a superconductor. It was first proposed by Russian physicist Alexander Andreev in 1964 [24].

When a normal metal and a superconductor are brought into contact, electrons from the normal metal with energies below the superconducting energy gap can penetrate into the superconductor as quasi-particles called Andreev reflected Cooper pairs. These pairs consist of two electrons with opposite momenta and opposite spins.

During Andreev reflection (Fig. 1.8), an incoming electron from the normal metal with energy below the superconducting energy gap is retro-reflected as a hole with opposite momentum and spin in the opposite direction. Simultaneously, a Cooper pair is created in the superconductor with opposite momentum and spin. This process conserves both energy and momentum. As a result of Andreev reflection, an intriguing phenomenon occurs near the NS interface. Cooper pairs have the ability to penetrate the adjacent normal metal region, effectively "popping in" to that region. This process leads to the emergence of a non-zero pairing amplitude within the confines of the normal metal

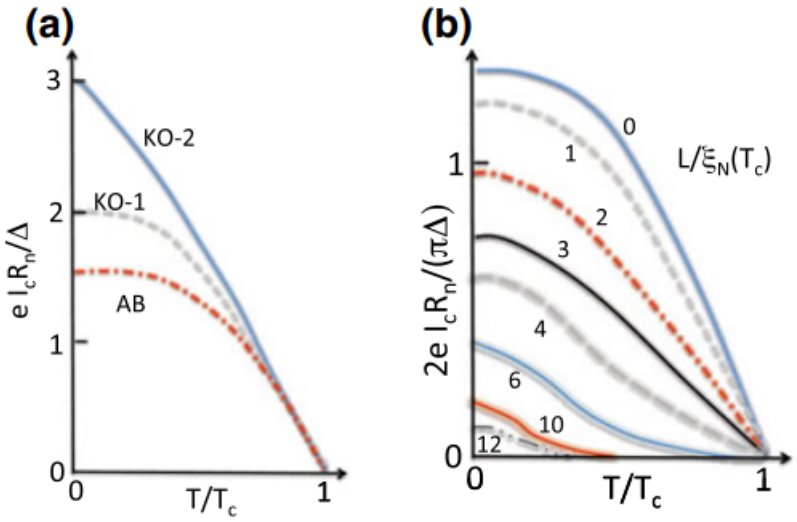

Figure 1.6: **a)** $I_cR_n(T)$ product as a function of the normalized temperature for Ambeagokar - Baratoff (**AB**), and Kulik-Omelanch (**KO1**,**KO2**) limits. **b)** The normalized $I_cR_n(T)$ value, is plotted for various values of the ratio between the barrier length L and ξ_N. Adapted from [23].

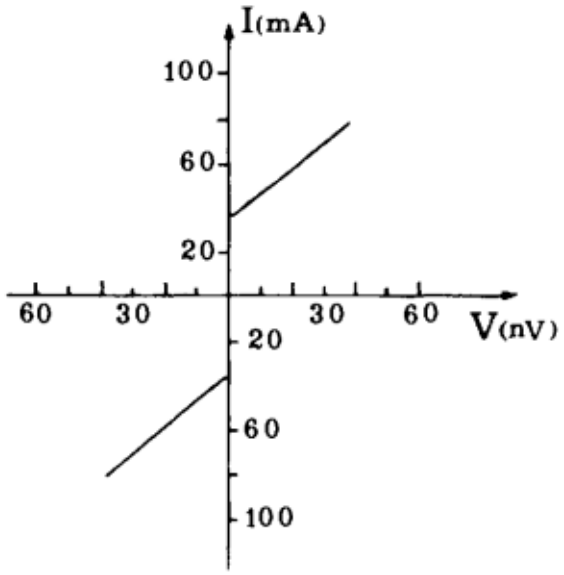

Figure 1.7: Current - Voltage Characteristic for a superconductor-normal-superconductor junction [25].

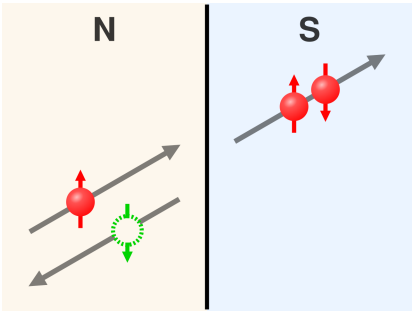

Figure 1.8: When an electron (colored in red) encounters the boundary between a standard conductor (labeled as N) and a superconductor (marked as S), it triggers the creation of a Cooper pair within the superconducting material. Simultaneously, in the normal conductor, a retro-reflected hole (depicted in green) is generated. The vertical arrows indicate the spin band in which each of these particles resides.

[19]. Conversely, an inverse effect is also observed. This physical phenomenon can happen multiple times, on both interfaces. In this case it is called Multiple Andreev Reflections (MAR). MAR occurs when an electron undergoes multiple Andreev reflections at the normal metal-superconductor interface. As a result, the electron keeps undergoing Andreev reflections, effectively tunneling through the interface multiple times.

The multiple reflections lead to interesting quantum interference effects. As an electron undergoes successive Andreev reflections, it accumulates a phase shift. Depending on the conditions, this can lead to resonant behavior, where the probability of an electron being transmitted is enhanced at specific energy levels. These levels are typically resonant energy levels within the gap, and electrons need to have energies that match these levels to exhibit resonant behavior and undergo multiple Andreev reflections [26].

Phenomenologically, what is observed in diffusive systems its a non-zero order parameter within the normal zone. In diffusive systems, Cooper pairs from a superconducting metal in close proximity diffuse into the normal metal [16], while electrons/hole diffuse into the superconducting material: this reciprocal phenomenon is referred to as the superconducting proximity effect. The extent of this penetration is characterized by the "**normal coherence length**" denoted as ξ, which can be calculated as $\xi = \sqrt{\frac{\hbar D}{2\pi k_B T}}$ (see for example [27]). For typical metal samples at a temperature of around 100 mK, the penetration depth ξ typically ranges from a few nanometers to hundreds.

A very important feature is that of being able to use the proximity effect to induce superconductivity in materials that show little or none, forming an hybrid system. In this case, the smaller the distance between the two superconducting leads of a Josephson junction, the greater the possibility of creating a junction. The valid reason for trying to induce superconductivity into a material that does not possess it concerns the possibility of adding this to an already vast list of useful properties, then exploiting one or more of these together with superconductivity. An example can be found in [28].

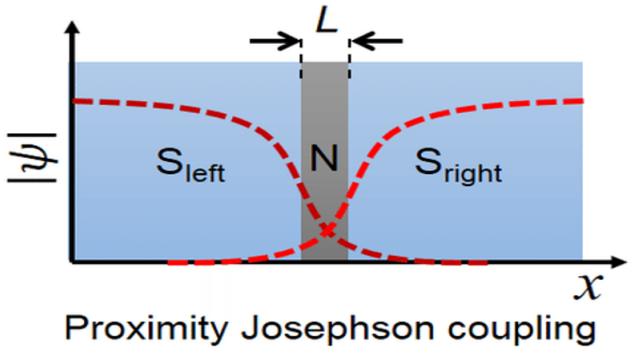

Figure 1.9: A sketch of the superconducting proximity effect in S-N-S junctions is shown. In red the superconducting order parameter of the left and right superconducting banks. If the N-layer is thin enough ($L < \xi_N$) and the transparency at the interface between the coupled materials is high, then the overlapping of the superconducting order parameters can take place.

Once the superposition of order parameters occurs effectively within the normal material as in Fig. 1.9, a super-current flows through the junction, of the type in Fig 1.7. Depending on the length L of the normal zone, which separates the two superconducting leads, different transport properties are observed. It is possible to demonstrate, for example for long junctions ($L \gg \xi$), that the critical current within these junctions follows this trend [23]:

$$\frac{eI_cR_n}{2\pi T_c} = V^* \frac{L}{\xi^*} e^{\frac{-L}{\xi^*}} \tag{1.17}$$

where V^* is a prefactor that can be calculated and $\xi^* = \xi_n \sqrt{\frac{T_c}{T}}$ (thus giving also a temperature trend) and it's the effective decay length. Moreover, an expression for the I_cR_n product for such structures is found [23] for $T = 0K$:

$$eI_cR_n = 20.64\pi T_c \left[\frac{\xi_n}{L}\right]^2 = 10.82E_{Th} \tag{1.18}$$

where $E_{Th} = \hbar\frac{D}{L^2}$ is the Thouless energy and is related to either the induced energy gap into the diffusive normal metal attached to the superconductor leads and to the dwell time the particles spends in travelling the interface between the superconductor lead and the normal region.

Let us now consider the case in which the inter-layer between the two superconducting regions has magnetic properties. As for the conventional BCS microscopic theory of superconductivity, Cooper pairs are composed of electrons with opposite spin [12]. However, in ferromagnetic materials, the spins tend to align in the same direction. This mean that when you bring a superconducting material (S) in close proximity to a ferromagnetic material (F) to form an S/F bilayer, you introduce two competing order parameters [29]: superconductivity, characterized by the formation of Cooper pairs and the presence of

a superconducting energy gap, and Ferromagnetism that is characterized by the alignment of electron spins and the presence of a large exchange field. An exchange field, also known as the exchange interaction or exchange coupling, refers to the interaction between electron spins in a material.

Since the energy scales associated with strong ferromagnetic substances are significantly larger than the typical energy scales of superconductivity, it is expected that superconductivity would be greatly suppressed in S/F bi-layers. The energy scale characterizing superconductivity is typically represented by the superconducting energy gap, which amounts to a few meV. In contrast, the typical exchange fields observed in strong ferromagnetic materials range from hundreds of meV to a few eV [30].

Due to this energy scale difference, the strong ferromagnetic order tends to disrupt the formation and stability of Cooper pairs in the superconducting material. The magnetic exchange interactions between electrons in the ferromagnetic material can break apart the Cooper pairs and suppress superconductivity. In essence, the strong ferromagnetic environment hinders the delicate balance of electron pairing required for superconductivity.

It is precisely based on the exchange field that in 1964, Larkin and Ovchinnikov [31] theorized that in a pure ferromagnetic superconductor at low temperatures, superconductivity could exhibit non-uniform behavior, featuring a modulation of the order parameter, as in Eq. 1.19 at the scale of the superconducting coherence length (known as the FFLO state) , of the type in the equation 1.19. This modulation in the superconducting order parameter arises from the Zeeman splitting of electronic levels, caused by the exchange field, while the two lengths (ξ_{F1}, ξ_{F2} depend on the model used and the transport regime considered [3, 32, 33].

$$\psi_s = \psi_{s_0} e^{-\frac{x}{\xi_{F1}}} cos\left(\frac{x}{\xi_{F2}}\right) \tag{1.19}$$

This oscillation arises due to changes in the nature of the Cooper pairs themselves. The conventional Cooper pairs are in a spin singlet state, but under the influence of a homogeneous exchange field, spin triplet correlations emerge [29]. This causes the Cooper pairs to become a mixture of the two states. The minority spin band has higher potential energy, resulting in a lower kinetic energy for electrons compared to the majority spin band. Consequently, the Cooper pair gains a net momentum, leading to oscillations in the space superimposed on an exponential decay. This behaviour can be observed in Fig. 1.10.

In a normal metal, superconductivity is also affected but to a lower extent. The significant factor there is the "temperature" ($k_B T$), which is much smaller than the exchange energy (E_{ex}) as previously said. This results in a larger distance (N) over which superconductivity survives compared to the shorter distance (F) in the ferromagnetic environment (F) as in Fig. 1.10. In fact, for this very reason in ferromagnetic junctions the length of the inter-layer is of different dimensions compared to that of normal materials. Replacing the normal metal with a ferromagnetic behaviour (F) introduces new factors like spin polarization (P) and exchange energy (E_{ex}) into the system. As a consequence, Andreev reflections are reduced as the mechanism is limited by the minority spin band.

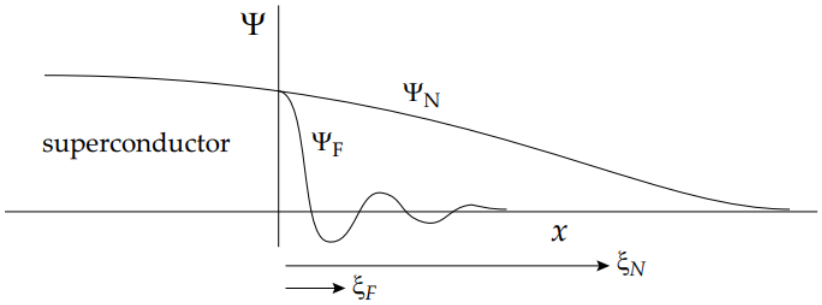

Figure 1.10: Proximity Effect in S/F junction. ξ_N and ξ_F are the two coherence lengths of respectively normal and ferromagnetic material [29].

1.2 Resistively Shunted Junction Model

1.2.1 General Model

In an ideal Josephson junction, the current I_J is accurately described by the expression $I_J = I_c \sin(\phi)$, where I_c represents the critical current. However, in real-world devices, factors such as the finite size of the superconducting films and the inevitable presence of leakage resistance in the oxide barrier necessitate a more comprehensive model. This extended model includes both shunt capacitance and resistance, as depicted in the equivalent circuit shown in Fig 1.11.

The total current flowing through this device comprises three components. Firstly, there is the super-current, which arises from the pairing of electrons (Cooper pairs) and is directly proportional to the sine of the phase difference ϕ. Secondly, there is a dissipative normal current I_R that flows through the resistance of the junction, introducing dissipative effects. Finally, there is a displacement current I_D that passes through the capacitor, accounting for the effects of the electric field and charge accumulation.

By considering these additional elements of shunt capacitance and resistance, the more comprehensive **Resistively Shunted Junction Model** (RCSJ) captures the behavior of a real Josephson junction, accounting for both the super-current and the dissipative effects through resistance, as well as the influence of the displacement current through the capacitor. Those are :

$$I_R = \frac{V}{R} = \frac{h}{2eR}\frac{d\phi}{dt} \tag{1.20}$$

$$I_D = C\frac{dV}{dt} = \left(\frac{\hbar C}{2e}\right)\frac{d^2\phi}{dt^2} \tag{1.21}$$

If a Josephson junction is biased from an external current source then:

$$\left(\frac{\hbar C}{2e}\right)\frac{d^2\phi}{dt^2} + \left(\frac{\hbar}{2eR}\right)\frac{d\phi}{dt} + I_c \sin(\phi) = I_{\mathrm{dc}} \tag{1.22}$$

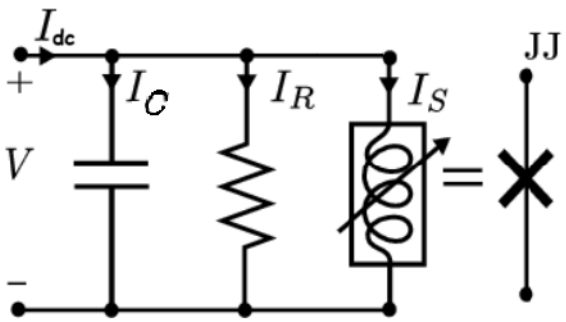

Figure 1.11: Circuit representation of the RCSJ model.

Consider the scenario where a Josephson junction is subjected to a gradually increasing direct current (dc) source, starting from zero. It becomes evident that as long as the external bias remains below the critical value I_c of the junction, the phase ϕ can adjust to a value that enables the entire bias to be carried solely by the Josephson element as a dc super-current, resulting in zero voltage across the junction. The shunt resistance and capacitance essentially serve as bypass components. However, once the bias reaches I_c, the sine of ϕ reaches its maximum value of unity. Any slight increase in the bias beyond this point induces oscillations in the junction. This dynamic state activates the other two branches in the equivalent circuit (shunt capacitance and resistance), causing a finite time-averaged voltage to abruptly appear across the device. This sequence of events is evident in the current-voltage characteristics of Josephson junctions as we will see in the next section.

Th Eq. 1.23 recall the equation (really similar to the one just found) governing the dynamics of a torque driven pendulum [34]

$$I\frac{d^2\theta}{dt^2} + b\frac{d\theta}{dt} + mgr\sin(\theta) = \Gamma \tag{1.23}$$

In the given equation, θ represents the angular coordinate of the pendulum bob, with mass m, positioned at a distance r from the axis of rotation. The term I represents the total moment of inertia of all rotating components of the pendulum, while b is a parameter that indicates the strength of frictional damping, which is dependent on the angular velocity of the pendulum.

The expression mgr corresponds to the critical torque required to elevate the pendulum by 90 degrees, and Γ denotes the net applied torque. The natural frequency of un-damped small amplitude oscillations is denoted as ω_0 and can be calculated using the formula:

$$\omega_0 = \sqrt{\frac{mgr}{I}} \tag{1.24}$$

This Eq. 1.24 quantifies the characteristic oscillation frequency of the pendulum system when the effects of damping and external torque are negligible. A term by term comparison of the electrical and mechanical equations provides the results shown in Table 1.4. The

Coordinate	Pendulum	Josephson junction
Pendulum angle	θ	Junction phase ϕ
Natural frequency (ω_0)	$\sqrt{\frac{g}{\ell}}$	$\frac{1}{\sqrt{LC}}$
Damping	b	$\frac{1}{RC}$
Forcing	Applied torque τ	Bias current I_{dc}
Critical forcing	$\tau_c = mg\ell$	I_c
Time dependence	$\dot{\theta} = \frac{d\theta}{dt}$	$V = 2e\frac{d\phi}{dt}$

Table 1.4: Comparison of pendulum and Josephson junction quantities.

counterpart of a Josephson junction's current-voltage characteristic in the context of a driven pendulum is a graph depicting the time-averaged angular velocity as a function of the applied DC torque. Looking at the classical analogue it is possible to better understand the dynamics and behaviour of the electronic system.

The behavior can be explained as follows: when the applied torque (drive current) is below the critical value (mgr) (critical current), the pendulum angle adjusts itself to a value that satisfies the equation $mgrsin(\theta) = \Gamma$. When the torque is slightly higher than the critical value, the angle θ exceeds 90 degrees, and the pendulum begins to spin in a pattern of alternating fast and slow oscillations. The average angular velocity (tension) settles at a finite value.

As the applied DC torque increases further, the spinning motion intensifies, and its time-averaged value also increases. Conversely, gradually decreasing the torque retraces the characteristic, but the system does not return to a static state when the critical torque (mgr) is reached again. This is because the spinning pendulum possesses momentum, causing the spinning state to persist until a lower torque value is attained. Similar to before, the system exhibits hysteresis.

1.2.2 Under-damped and Over-dumped Regime

Significant insights into the nonlinear dynamics of the junction can be obtained by expressing the Eq. 1.22 in terms of an effective potential called "washboard potential" $U(\phi)$:

$$U(\phi) = -E_J \cos(\phi) - \frac{\hbar I}{2e}\phi \tag{1.25}$$

where $E_J = \frac{\hbar Ic}{2e}$ is the Josephson energy. This allows describing the dynamics of a Josephson junction through the motion of a particle representing the phase difference along the potential $U(\phi)$ (Fig. 1.12). Imagine a particle situated in one of the potential wells. As the bias current increases, the washboard potential becomes tilted. The phase particle stays within the minimum until the bias current is equal to the critical current, but once the bias current becomes greater than the critical current, it starts rolling along the washboard. The "running state" of the particle, corresponds to the existence of a finite voltage across the junction. The particle's motion is governed by the interplay between

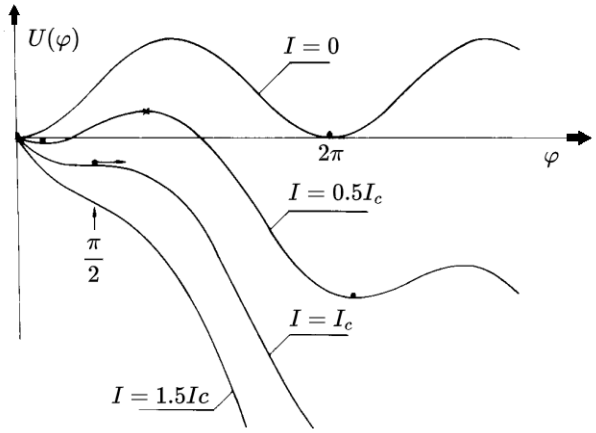

Figure 1.12: Potential energy U of the current-biased Josephson junction at various values of the bias current. Adapted from [27].

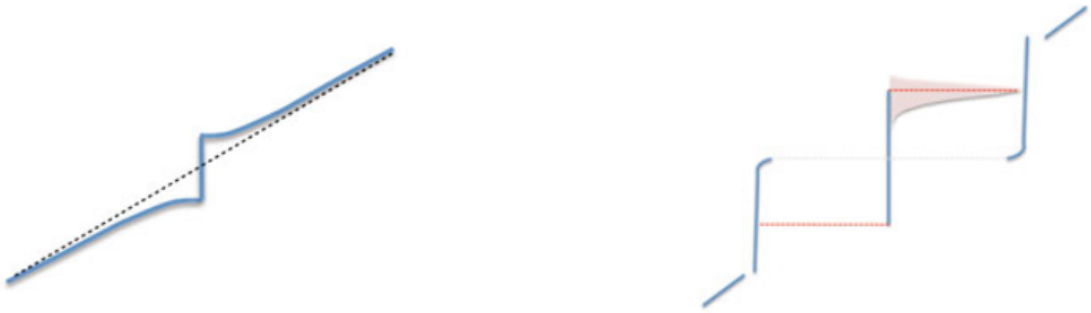

Figure 1.13: **Left**: Current-Voltage Characteristic for an over-dumped junction. **Right**: Current-Voltage Characteristic for an under-dumped junction [23].

the gravitational-like term $-E_J \cos(\phi)$ and the linear term $-\frac{\hbar I}{2e}\phi$. The potential landscape influences the particle's behavior, leading to various dynamical phenomena such as oscillations, periodic motion, or even the particle becoming trapped in potential wells. In general, the RCSJ model can be divided into two regimes: over-damped and under-damped, depending on the behavior of the phase within a single well of the potential. Suppose we initially drive the phase to a value θ_0 using an external current and then abruptly turn off the external current. If θ_0 is not equal to $2n\pi$, which corresponds to a minimum of $-E_J \cos(\phi)$, the phase initiates a damped oscillation within this potential, gradually approaching the potential minimum. In the under-damped regime, the phase undergoes multiple oscillations before decaying into the minimum, while in the over-damped regime, the decay time is shorter than the oscillation period.

In the **over-damped regime**, at a non-zero temperature, there is a finite probability for the junction to "escape" (see [19]) into a finite-voltage state at a lower current than Ic. This effect smoothens the resulting $I - V$ curve and reduces the measured critical current

below Ic.

In the **under-damped regime**, when the quality factor (Q) is much larger than $\frac{1}{2}$, we are in presence of large capacitance and low dissipation, the $I-V$ curves of the Josephson junction exhibit hysteresis. Upon increasing the current (I_{dc}) from zero, the junction remains in a super-current-carrying state until reaching a current close to I_c, the critical current. At this point, the junction undergoes a discontinuous jump (at $T = 0$) to a finite voltage close to $2\Delta/e$, where Δ represents the superconducting energy gap.

When the current I is subsequently reduced, the junction does not immediately return to the zero-voltage state before the current reaches a re-trapping current, denoted as I_r.

1.3 Magnetic Field and Current Patterns

In this section it will be described the electromagnetic behavior of a Josephson junction in a magnetic field (Fig. 1.14), when an external magnetic field B is applied, orthogonal to the transport direction. What happens is the interference of the Cooper pair wave functions, which change the transport properties of the junction. This phenomena collaborate to generate a spatial variation of the critical current density along the junction barrier, resulting in specific characteristics in the magnetic dependence of I_c and the $I-V$ curves. Referring to the general equation that relates the phase, electric current, and magnetic field:

$$\vec{\nabla}\phi = \frac{2e}{\hbar}\left(\frac{m\vec{J}}{2e^2\rho} + \vec{A}\right) \tag{1.26}$$

where ρ is the density of Cooper pairs and $\vec{A}$ is the vector potential. The influence of the bulk super-currents J can be disregarded as they are either orthogonal to the integration boundary or insignificantly small within the interior of the superconductors. A magnetic field $B = B_y(x,z)\hat{y}$ is applied to the junction, and it permeates the electrodes on the scale of London penetration depths λ_L and λ_R (L and R denote the left and right regions respectively). The calculation of the gauge-invariant phase difference between two points along the barrier with coordinates x and $x + dx$ demonstrates the impact of the externally imposed magnetic field.

$$\phi(x+\Delta x) - \phi(x) = \frac{2e}{\hbar}\oint \vec{A}\cdot\vec{dl} \tag{1.27}$$

By using the Stokes' theorem, taking the limit $\Delta x \to 0$ one obtain the following equation:

$$\frac{\partial\phi}{\partial x} = \frac{2\pi B_y d}{\Phi_0} \tag{1.28}$$

where B_y is the local magnetic induction, and $d = t + \lambda_L + \lambda_R$. Integrating the last equation yields:

$$\phi = \frac{2eB}{yd}x + \phi_0 \tag{1.29}$$

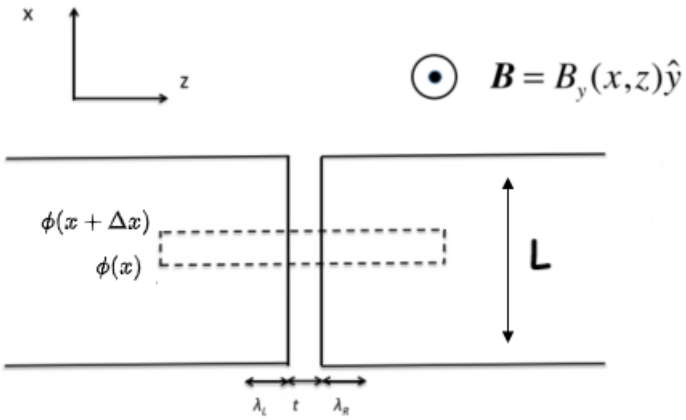

Figure 1.14: Geometric Configuration of the Junction: Two superconducting layers are spaced apart by a slender insulator with a thickness denoted as "t". Within this setup, there exists a magnetic field with the induction represented as $B = B_y(x, z)\hat{y}$, which extends a short distance into the left superconductor, characterized by the penetration depth λ_L, and also into the right superconductor with a penetration depth of λ_R. The dashed line serves as an integration contour for analysis.

The Josephson equation than becomes :

$$J_s = J_c \sin\left(\frac{2eB}{yd}x + \phi_0\right) \tag{1.30}$$

and by integrating over all the junction width the supercurrent for a rectangular junction we have a Fraunhofer pattern as illustrated in the Fig. 1.15 (left):

$$I_s(\Phi) = J_s W L \left| \frac{\sin\left(\pi \frac{\Phi}{\Phi_0}\right)}{\pi \frac{\Phi}{\Phi_0}} \right| \tag{1.31}$$

While for a circular junction [25]:

$$I_s(k) = \pi R^2 J_s \left| \frac{J_1(kR)}{\frac{1}{2}(kR)} \right| \tag{1.32}$$

where $k = \frac{2\pi d}{\Phi_0} H$ and J_1 is the Bessel Function. A qualitative sketch can be looked at in Fig. 1.15 (right).

These are examples of cases in which the current can be calculated analytically, in the experimental case however, various factors can influence this figure, the shape of the junction, characteristics of the electrodes or the barrier, and even their potential irregularities contribute to unique phase variations across the barrier, leading to Meissner screening magnetic interference effects, the creation and entrapment of vortices (normal

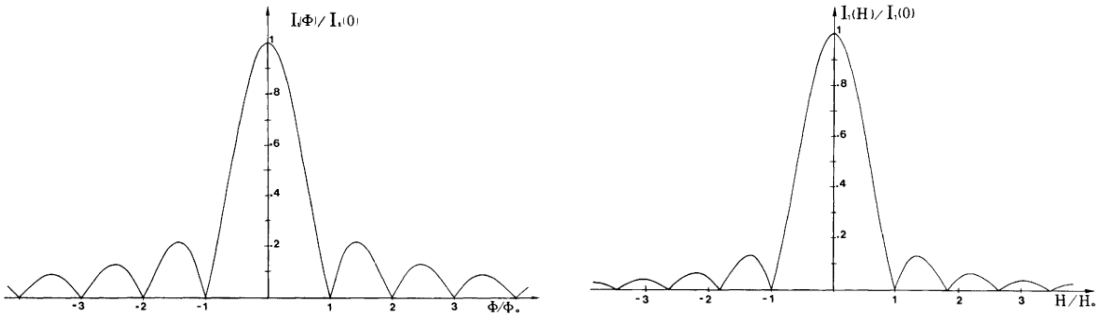

Figure 1.15: **Left** : Critical current vs Flux through a rectangular junction. **Right** : Critical current vs Magnetic filed applied on a circular junction [25].

region into the superconductor), shielding, and spontaneous super-currents [19]. All these phenomena contribute to a change of the shape and a modulation of the current amplitude or even an horizontal translation, if a magnetic field is already present into the junction.

1.3.1 SFS Magnetic Pattern

In SFS Josephson junctions, aside from the effects that can also be observed in non-magnetic junctions, various other intriguing phenomena come into play. Among these, the most important is the introduction of an extra flux into the junction due to the magnetization of the F-layer below the Curie temperature T_{Curie}.

In Josephson junctions (JJs) containing a ferromagnetic (F) barrier, the evaluation of the total magnetic flux through the junction, denoted as Φ, requires consideration of the flux contributed by the magnetization of the F layer. This flux, Φ_F, is given by:

$$\Phi_F = \mu_0 M_F L d_F, \tag{1.33}$$

where: μ_0 is the permeability of free space, M_F is the magnetization of the F layer, L is the cross-sectional width of the JJ, and d_F is the thickness of the F layer.

Hence, the total magnetic flux through the junction can be expressed as:

$$\Phi = \mu_0 H L d_m + \mu_0 M_F L d_F, \tag{1.34}$$

where d_m represents the thickness of the material penetrated by the applied magnetic field, given by:

$$d_m = 2\lambda_L + d_F \quad . \tag{1.35}$$

Due to the magnetic hysteresis of the F layer, the critical current (I_c) versus applied magnetic field (H) curves exhibit hysteresis behavior that depends on the direction of sweeping the magnetic field. Specifically, as H is swept from positive to negative fields (down curve), the Fraunhofer-like pattern is expected to shift towards negative fields due

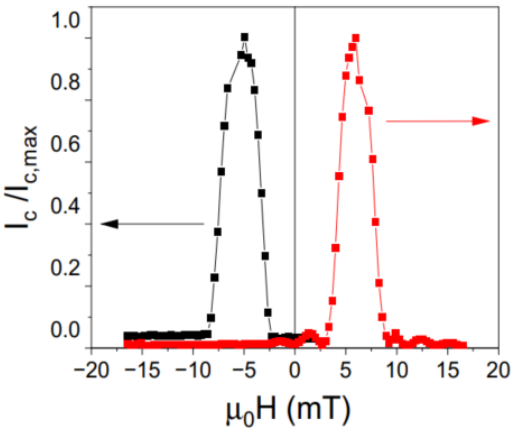

Figure 1.16: Magnetic JJs's hysteresis behavior concerning the $I_c/I_{c_{max}}$ versus H curve obtained through the application of a magnetic field. The black and red curves represent the magnetic response when the magnetic field is directed downward and upward, respectively, during the magnetic rewriting process. Adapted from [2].

to the positive remanence of the ferromagnet. Conversely, when the field is swept from negative to positive fields (up curve), the pattern shifts towards positive fields 1.16.

In the simplest case of a homogeneous F barrier in a single-domain state, we can assume that [3] $\mu_0 M_F \approx \mu_0 M_s \approx \mu_0 M_r$, where: M_s is the saturation magnetization (maximum achievable), and M_r is the remanent magnetization (when $H = 0$ after being magnetized). In this scenario, the Fraunhofer pattern is offset by a factor given by [3]:

$$\pm\mu_0 H_{\text{shift}} = \mp\mu_0 M_s d_F / d_m. \tag{1.36}$$

1.4 SIsFS Josephson Junctions

Superconducting Josephson junctions (JJs) with metallic barriers (SFS JJs) typically exhibit over-damped behavior. However, by introducing ferromagnetic layers coupled with insulating barriers (SIsFS or SIFS JJs), it's possible to engineer JJs with high-quality factors and under-damped characteristics. The properties of SIsFS structures can be explained using a microscopic model, considering materials in the dirty limit and assuming finite transparency at the bi-layer interface [35]. The Josephson effect in these junctions can be described using Usadel equations and Kupriyanov-Lukichev boundary conditions. Essentially, we can identify three distinct operational modes by comparing the thickness of the "s" layer (denoted as "d_s") to the critical thickness (referred to as "d_{sc}") [3]. This critical thickness represents the minimum required thickness of the "s" layer within an "sF" bi-layer for superconductivity to persist at a specific temperature. The three modes are:

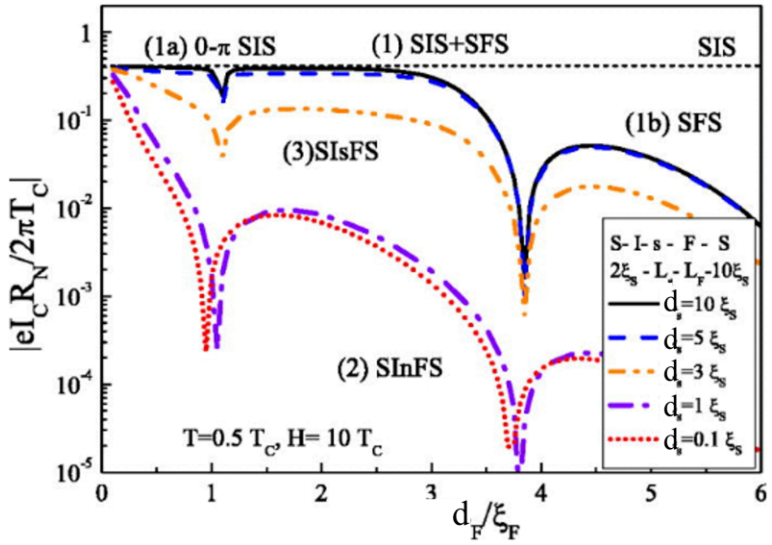

Figure 1.17: The characteristic voltage I_cR_N of the SIsFS structures as a function of the F layer thickness d_F for various thicknesses of the intermediate superconducting film d_s at $T = 0.5\ T_c$. The short-dashed straight line illustrates the I_cR_N product of the tunnel SIS junction under the same temperature conditions [35].

1. When d_s is significantly greater than d_{sc}, the pair potential within the s layer (Δ) closely approximates that of the bulk material. In this scenario, the SIsFS structure can be modeled as a combination of a tunneling SIs JJ and a ferromagnetic sFS JJ. For the first mode, a classification based on d_F can be done :

   - In the case of a small d_F and when I_c^{SIs} is much smaller than I_c^{sFS},the I-V curve of the overall SIsFS device is primarily determined by its SIs component. This results in the I_cR_N product reaching its maximum value, similar to that of a standard SIS JJ. Simultaneously, the phase difference φ in the ground state of an SIsFS junction is influenced by the sFS component. Consequently, both 0 and π states can be achieved, depending on the thickness of the F layer, denoted as d_F.
   - When d_F has a large value, the structure transitions into a standard SFS junction without any influence from the barrier.

2. In cases where d_s is less than d_{sc}, the absence of superconductivity in the s interlayer leads to the creation of a complex weak link region known as "complex-InF," where 'n' signifies the intermediate s film in its normal state. This results in I_cR_N values that are on the order of SIFS Josephson junctions.

3. When d_s is approximately equal to $d_{sc} \approx 3\xi_s$, the properties of the structure become highly sensitive to d_F and the exchange field of the F layer. These parameters

regulate the suppression of superconductivity within the sF bi-layer. This suppression, in turn, adjusts the effective transition temperature T_c, which corresponds to the transition temperature of the sF inter-layer and leads to the emergence of a proximity-like tail in the $I_c R_N(T)$ dependence.

In Fig 1.17 is examined the $I_c R_n$ for different F-layer thicknesses with a reference tunnel JJs, indicated by the dashed line. Various scenarios emerge, such as when the middle s' layer is much thicker than the s layer, resulting in a series of SIs' and s'FS junctions. In some cases, the structure behaves like a switchable $0 - \pi$ SIS junction or transforms into a standard SFS junction.

–2–
Experimental Set-Up

In this chapter I describe the setup used to characterize the Josephson junctions studied with a cryostat capable of reaching a base temperature of 10 mK, equipped with electronics used for the electromagnetic characterization of the junctions.

2.1 Dilution Refrigerator

The transport measurements have been carried out in the low temperature Lab of the University of Naples. It has been used the Triton Dilution Refrigerator, a state-of-the-art cryogenic system by Oxford Instruments, able to achieve extremely low temperatures, specifically 10 mK in 24 h [36].

The main components of the Triton system are shown in Fig. 2.1:

- **Cryostat with pulse-tube cooler**: The cryostat (Fig. 2.1 (A)) is the main vessel that houses the cooling system of the Triton. It provides a low-temperature environment for conducting experiments. It is equipped with a pulse-tube cooler, which utilizes oscillating pressure waves to compress and expand a gas, thereby achieving cooling through the Joule-Thomson effect.

- **Gas handling and control rack**: The gas handling and control rack (Fig. 2.1 (B)) is responsible for managing the flow and distribution of the helium gas mixture within the Triton system. It includes various valves, regulators, and sensors that control the gas pressure, flow rate, and other parameters. This rack allows for precise control and monitoring of the gas throughout the cooling process.

- **Pump rack**: The pump rack (Fig. 2.1 (C) consists of pumps that are used to circulate the helium gas within the Triton system. These pumps facilitate the circulation of the gas mixture, maintain the desired pressure levels, and ensuring efficient heat transfer within the system. The pump rack is an essential component for the proper functioning of the dilution refrigerator stage.

Figure 2.1: Triton consists of six stand stand-alone components: cryostat with pulse-tube cooler (A); gas handling and control rack (B); magnet power supply rack (if required) (C); pump rack (D); pulse-tube compressor (E) and a liquid nitrogen dewar with cold trap (F) [36].

- **Pulse-tube compressor**: The pulse-tube compressor (Fig. 2.1 (E) is a key element of the Triton system. It compresses the helium gas mixture, using ^3He , to higher pressures required for the cooling process. By compressing the gas, the pulse-tube compressor helps to increase the density and enhance the cooling efficiency as the gas passes through the heat exchangers.

- **Liquid nitrogen dewar with cold trap**: The liquid nitrogen dewar serves as a reservoir for storing and supplying liquid nitrogen (Fig. 2.1 (F). It provides a source of cryogenic cooling, typically at temperatures around 77 Kelvin (-196 degrees Celsius). The cold trap, located within the dewar, is used to capture and remove any impurities or unwanted gases present in the helium gas mixture. It helps ensure the purity and quality of the gas used for cooling.

The key component of the Triton Dilution Refrigerator is the dilution refrigerator itself. This type of refrigerator operates on the principle of cooling a sample by diluting a mixture of isotopes, ^3He and ^4He, and exploiting the cooling effect of their phase separation [36]. The initial cooling stage of the Triton Dilution Refrigerator involves the use of a pulse-tube cooler (A). This stage brings down the system's temperature to around 4 Kelvin. The pulse-tube cooler controls pressure waves to compress and expand a gas, resulting in cooling and heat removal. The dilution unit (DU) allows for the condensation of the helium gas mixture into a liquid state, achieving high pressures and low temperatures. It is characterized by the still, some heat exchanger and the mixing chamber as in Fig.

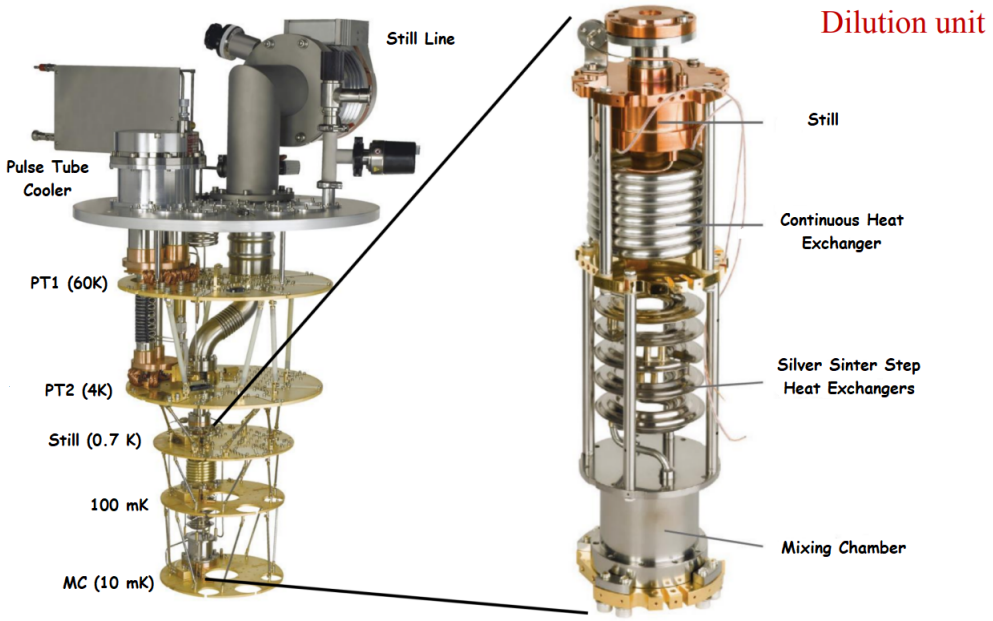

Figure 2.2: The crysotate with the temperatures of each stage and the main cooling lines on the left, while on the right a zoom of the dilution unit [36].

2.2. The dilution refrigerator stage is utilized to achieve extremely low temperatures. It involves a mixture of ^3He and ^4He isotopes. By carefully controlling the dilution process, the mixture undergoes phase separation in the mixing chamber, with ^3He becoming superfluid while ^4He remains in its normal state. This phase separation creates an environment of extremely low temperatures, reaching as low as a few millikelvin (thousandths of a Kelvin).

The condensation process of the ^3He gas is achieved using the Joule-Thompson (JT) stage. This stage comprises a highly efficient heat exchanger positioned within the still pumping line (right in Fig. 2.2) and an impedance where the gas can experience isenthalpic expansion. Being more specific, inside the still, a heat exchanger cools the returning ^3He liquid before it reaches the continuous counter-flow tube-in-tube heat exchanger (top - right in Fig. 2.2). The continuous heat exchanger further cools the ^3He to below $0.1K$. Following this, the ^3He passes through several step heat exchangers composed of discrete blocks of sintered silver with internal flow channels.

Finally, the ^3He enters the mixing chamber where dilution cooling takes place due to the enthalpy difference between the concentrated (incoming) and diluted (outgoing) liquid. While the incoming liquid is nearly pure ^3He, the diluted liquid predominantly consists of ^4He with a small fraction of ^3He. The diluted ^3He flows from the mixing chamber to the still, where it is preferentially evaporated and circulated by the pumping system.

2.1.1 Filters

When conducting experiments at such low temperatures, the measurements can be extremely sensitive to external influences or noise. Noise refers to unwanted signals or disturbances that can interfere with the accuracy of the measurements, sources of noise can include thermal fluctuations, electronic interference, and other environmental factors. Because the measurements mainly involve studying quantum effects, a high level of accuracy is essential. Any noise in the measurements can distort the results and make it difficult to extract meaningful information about the properties being studied. For the just mentioned reasons, a series of filters is used to attenuate the signal of unwanted frequencies. From top to bottom of the cryostat the filters installed are :

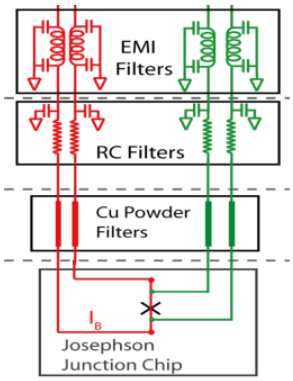

Figure 2.3: Schematic of the filters used in the Tryton system.

- **EMI Filters** (Electromagnetic Interference Filters):
  EMI filters (Fig. 2.4) are designed to attenuate electromagnetic interference (EMI) that can affect the performance of electronic devices at room temperature. EMI can be generated by various sources, such as power lines, radio frequency signals, or other electronic equipment. These filters work by impedance matching and frequency-dependent attenuation, reducing the level of unwanted electromagnetic noise before it reaches the sensitive components of the electronic system. EMI filters typically consist of passive components, including capacitors, inductors, and resistors, arranged in a specific configuration. In our case, the compontens are

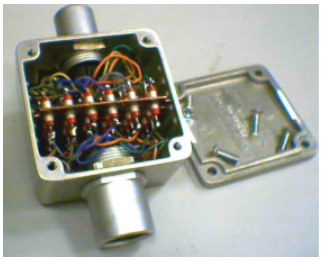

Figure 2.4: EMI filters installed on the Tryton system are shown.

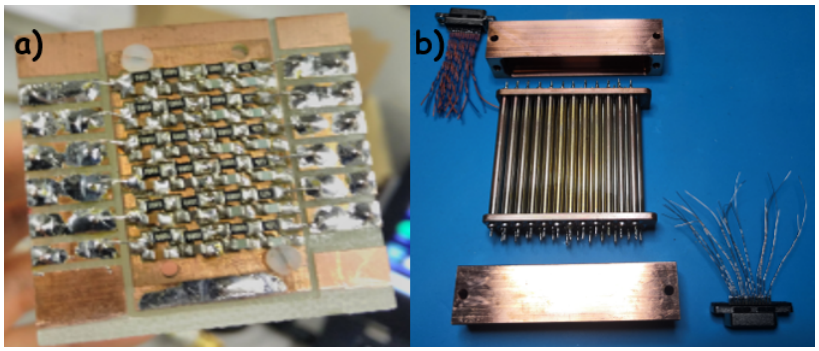

Figure 2.5: **a)** Image shows a series of RC filters used for DC lines in the Tryton system.**b)** Assembly of copper powder filters.

arrenged in such a way to form Pi-filters. Pi-filters consist of two capacitors and one inductor, arranged in the shape of a "π". The purpose of these filters is to provide high-frequency noise filtering and attenuation, therefore operating as low-pass filters.

- **RC Filters**
  In a low-pass RC filter, the resistor is connected in parallel to the input signal, and the capacitor is connected in series with the output, as in Fig 2.5. This configuration allows lower-frequency components to pass through while attenuating higher-frequency components. The cutoff frequency determines the point at which the filter starts attenuating the signal. In our case, they consist of two capacitors with a capacitance of $1nF$ and a resistor with a resistance of 100Ω, resulting in a cutoff frequency of 1.6 MHz. They represent the second stage of filters and are located at the still plate ($4K$). It's worth noting that the actual performance of an RC filter may be affected by factors such as component tolerances, temperature variations, and impedance interactions with the load and source. Therefore, for more precise or demanding filtering requirements, the Pi-filters are being used together with the RC filters.

- **Copper Powder Filters**
  Copper powder filters Fig. 2.5, also known as copper mesh filters or copper powder sintered filters, are a type of porous filter made from copper particles or copper powder. This type of filters are manufactured by compacting and sintering copper powder particles together to form a solid and porous structure. The sintering process involves heating the copper powder to a temperature below its melting point, causing the particles to bond together and create a network of interconnected pores. In our case they are made of a Spiral coil of insulated wire inside a tube filled with copper powder with a grain size ranging from 5 to 30μm, thus the effective surface area is enormous. They have a cutoff frequency in the order of several GHz and are positioned at the cold plate ($100mK$). They are used because of their conductivity properties such as electromagnetic shielding, EMI/RFI filtering, and

grounding applications.

The cryostat DC line's setup consists of a total of 24 filtered lines, divided into 12 lines for current signals and 12 lines for voltage signals. As the electrical signal progresses through the cryostat's various plates, it encounters lines of various materials. For current signals, copper is utilized from room temperature down to the $4K$ stage. Beyond that point, up to the mixing chamber, NbTi is employed due to its superconducting properties, resulting in minimal dissipation of energy. In the case of voltage signals, the lines are composed of manganin, extending from room temperature down to the mixing chamber.

2.1.2 Cryostat Temperature Control

<table>
<tr><th>Setpoint [K]</th><th>P</th><th>I</th><th>D</th><th>Heater Range</th><th>Sensor Type</th><th>Sensor Excitation</th><th>Turbo State</th></tr>
<tr><td>0.1
0.2
0.3
0.4
0.5
0.6
0.7
0.8
0.9
1.0</td><td rowspan="2">15</td><td rowspan="2">120</td><td rowspan="2">0</td><td rowspan="2">10 mA</td><td rowspan="2">RuOx</td><td rowspan="2">632 μV</td><td rowspan="2">ON</td></tr>
<tr><td>1.2
1.4
1.6
1.8
2.0
2.5</td></tr>
<tr><td>1.2
1.4
1.6
1.8
2.0
2.5</td><td rowspan="2">3</td><td rowspan="2">10</td><td rowspan="2">0</td><td rowspan="2">3.16 mA</td><td rowspan="2">CERNOX</td><td rowspan="2">2 mV</td><td rowspan="2">OFF</td></tr>
<tr><td></td></tr>
</table>

Figure 2.6: Lakeshore bridge setting in the temperature range: 0.1 to 2.5 K [36].

The Tryton system offers the flexibility to set the measurement temperature acting on its pumps and heathers via the Lakeshore Bridge software.

The Lakeshore bridge will by default temperature control using the 'autoscanmode', meaning it will PID (in the context of control systems, PID stands for Proportional, Integral, and Derivative) control on one channel while intermittently reading the remaining channels. Each channel represents a certain temperature sensor, which operates efficiently in a certain temperature range, placed on different plates of the cryostat. By combining the proportional, integral, and derivative terms, the PID controller adjusts the control output.

The specific values of the P, I, and D terms are typically adjusted or tuned to optimize the control performance. The following table 2.6 gives an example of how to adjust the settings of the Lakeshore Bridge and the pumps in order to obtain the desired temperatures up to $2.5K$.

2.2 Measurement Techniques

One of the main experimental activities carried out during my thesis is the measurement of the current-voltage characteristics of Josephson Junctions as a function of temperature and magnetic field. To perform these measurements, an experimental set up was used, using all or a part of the instruments described in the appendix D.

2.2.1 Current vs Voltage Measures

The electrical signal, a triangular low frequency ($10Hz$) curve, is generated by the arbitrary wave function generator, connected in series with a tunable resistance, generally very high ($1\ M\Omega$), thus allowing the chip to be driven in current. After the resistance, the signal passes through a series of filters placed onto the cryostat, described in paragraph 2.1.1, in order to avoid unwanted frequencies, and then the signal reaches the DUT. Once the signal reaches the DUT, the output is then transmitted to the voltage and current pre-amplifiers placed at the output of the cryostat lines. The pre-amplifiers filter the signal through low pass filters (usually $3KHz$) and amplify it, which based on the amplitude of the signal and the off-set. The output signal from the pre-amplifiers is then transmitted to the HDO6000 (Teledyne) type oscilloscope, from which the reading takes place. The number of points taken by the oscilloscope is a function of two parameters: the sampling frequency (Max $2.5GHz$) and the time window in which the signal is collected. In general, since our signal has a low frequency there is no need for a high sampling frequency, making the choice of the number of points fall on 10,000 or 50,000. These points are saved from the oscilloscope interface and then the data analysis is performed on the current and voltage traces just saved in combination with an excel file using a custom Matlab script, which can be found in the appendix B. The chosen signal amplitude is fixed by maximizing its resolution, hence it changes based on the DUT and the temperature of the measurement. During the measurement, particular attention has to be paid to the parameters of the pre-amplifiers too, which require a suitable choice of amplification (as high as possible in order to maximize the signal-to-noise-ratio, but not as high as to reach the threshold). All amplification factors and filters used are recorded in the excel file used for the analysis.

The measurements that are carried out with this configuration of instruments are made using 4 probes, which is particularly useful in order to remove the contacts and lines resistance contribute (see appendix C for details).

An example of a measure performed with this on an Aluminum nanowire is shown in Fig 2.8. Using a threshold value and a tolerance value it is possible to evaluate the critical current value. Furthermore, through a linear fit the resistance of the normal branch is evaluated.

It's essential to remember that every measurement in physics inherently carries a degree of uncertainty or error. This uncertainty arises from various sources, including the precision of the instruments used, environmental factors, and the inherent stochastic nature of physical processes.

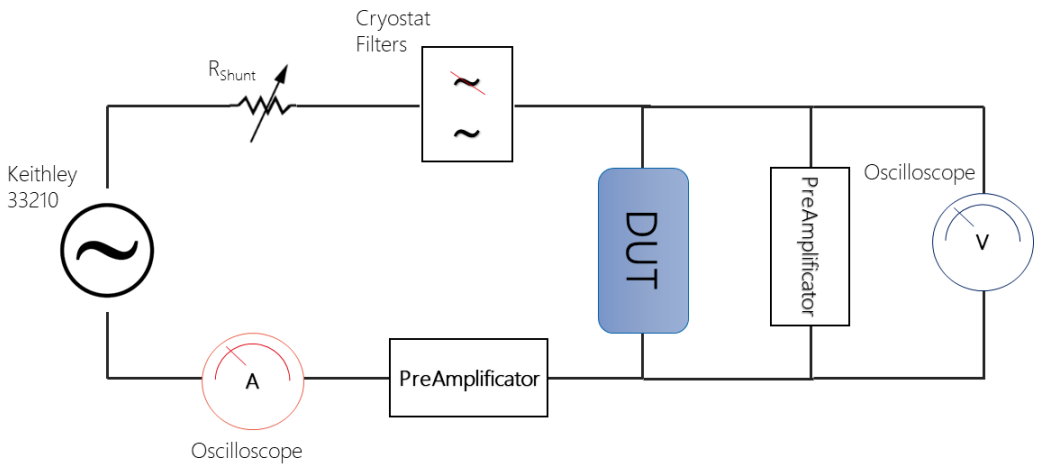

Figure 2.7: Electronic schematic of the measuring apparatus. The signal is generated passes through a shunt resistor and the cryostat filters and reaches the electronics at room temperature, consisting of a pre-amplifier and an oscilloscope.

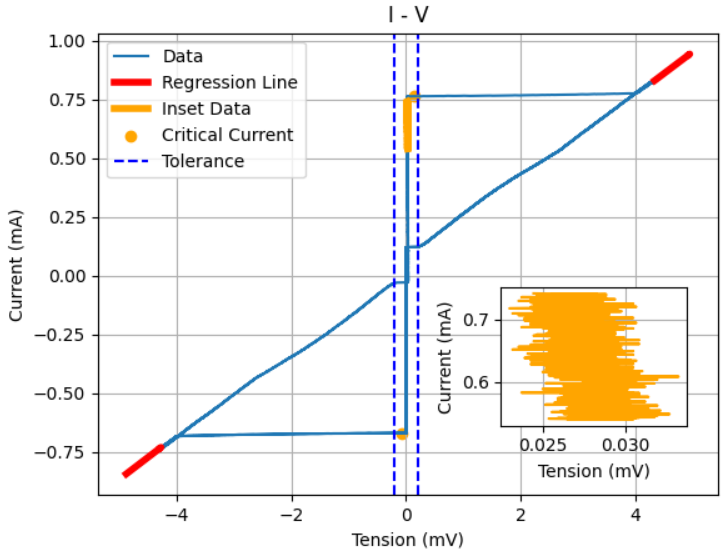

Figure 2.8: Current-voltage characteristic of an aluminum nanowire 10 μm long, 300 nm wide and about 100 nm high. The red line represents the data used for linear fit and normal resistance estimation. The vertical dotted lines represent the range chosen for evaluating the critical current. The data highlighted in yellow represents that shown in the inset.

In this specific measurement, the error associated with the current and voltage values is estimated to be approximately 1%. This estimation is derived from a careful analysis of the current and voltage curves recorded over time with the Oscilloscope. The 1% error indicates that for any given data point on the IV curve, the measured current or voltage value could deviate from the true value by up to 1% in either direction.

2.2.2 Current - Voltage as a Function of the Magnetic Field

Josephson junctions can exhibit exotic phenomena, such as the Fraunhofer diffraction pattern in their current-voltage characteristics, which arises due to their wave-like behavior when a magnetic field is applied to the junction, as already described in chapter 1. Thanks to these measurements it is possible to obtain important values, such as the magnetic penetration length, based on the periodicity of the pattern of the critical current.

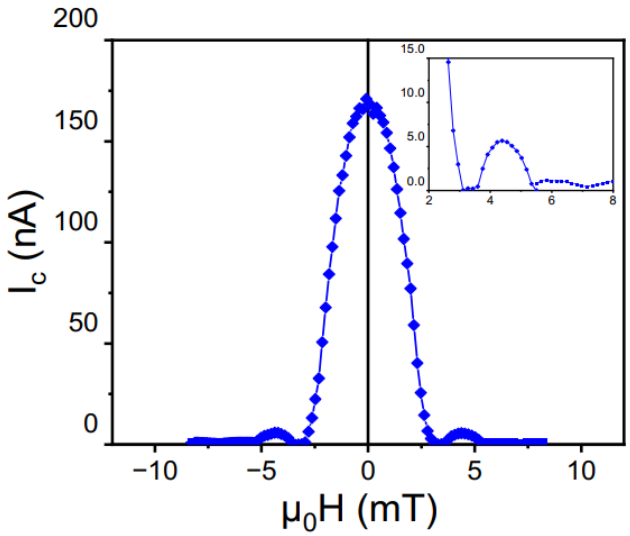

Figure 2.9: Example of measurement of the critical current for different values of applied magnetic field in the case of a SIS junction. An inset of the first zero of the function is shown at the top right. Adapted from [18].

In order to apply a magnetic field, a current is passed through a solenoid to generate a uniform magnetic field on the chip, with a conversion factor of 0.1 T/A. At each specific magnetic field value, the current - voltage characteristics are recorded with a LabView program, in the same manner as the one outlined in the previous section. Specifically, the critical current is evaluated for each curve. An example is represented in Fig. 2.9 . By following this procedure, in the event that a ferromagnetic material is present inside the JJ, it is possible to derive both the hysteresis curve of the magnetization of the material and the behavior of the critical current for different values of the magnetic field. For further details, see the measurements in chapter 4.

2.2.3 Conductance - Voltage measurements

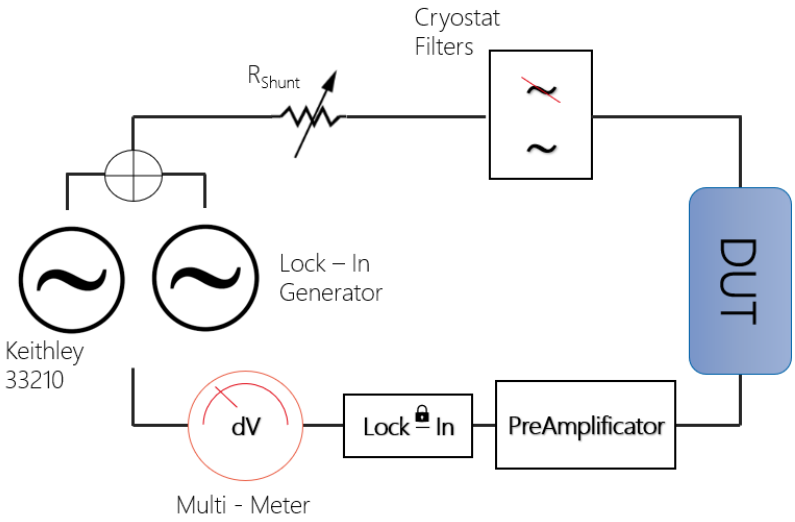

Figure 2.10: Simplified path of the current or voltage signal in conductance measurements.

Conductance measurement offers further details on the physics of the system under examination. Through the conductance divergence it is possible to estimate the value of the superconducting gap of the system, as already described in chapter 1, for various temperatures. Furthermore, the behavior of the conductance for values lower than the gap can give us an indication of the presence of all transport mechanisms, related to the presence of quasi-particles. Experimentally, for the conductance measurements the setup is schematized in Fig 2.10. The input current consists of a combination of two signals: a triangular ramp with a low frequency of $1.123mHz$ and a small sinusoidal excitation around $30Hz$. The ideal proportion between the amplitudes of these two signals is approximately 10^{-3}. To measure the output signal, a lock-in amplifier is employed. By fixing the reference frequency on the front panel, together with the pass-band filter having the same frequency as the central frequency, only the higher frequency $\nu(t)$ of the two contributes arrives to the read output signal (Eq. 2.1), giving a quick estimate of the signal variation compared to the almost fixed low frequency one.

$$V(t) = V_{LF}(t) + \nu(t) \quad \longrightarrow \quad V(t) \approx \nu(t) \tag{2.1}$$

The output signal coming from the lock in amplifier is then read using a multi-meter. An example of such a measurement is represented in Fig. 2.11. Since the conductance is given by the ratio of the variation of the current dI and the variation of tension dV, these two are measured with the aforementioned method and, by changing the point around which the low frequency signal is stationed, it is possible to obtain the conductance graph, collecting many points around each single value.

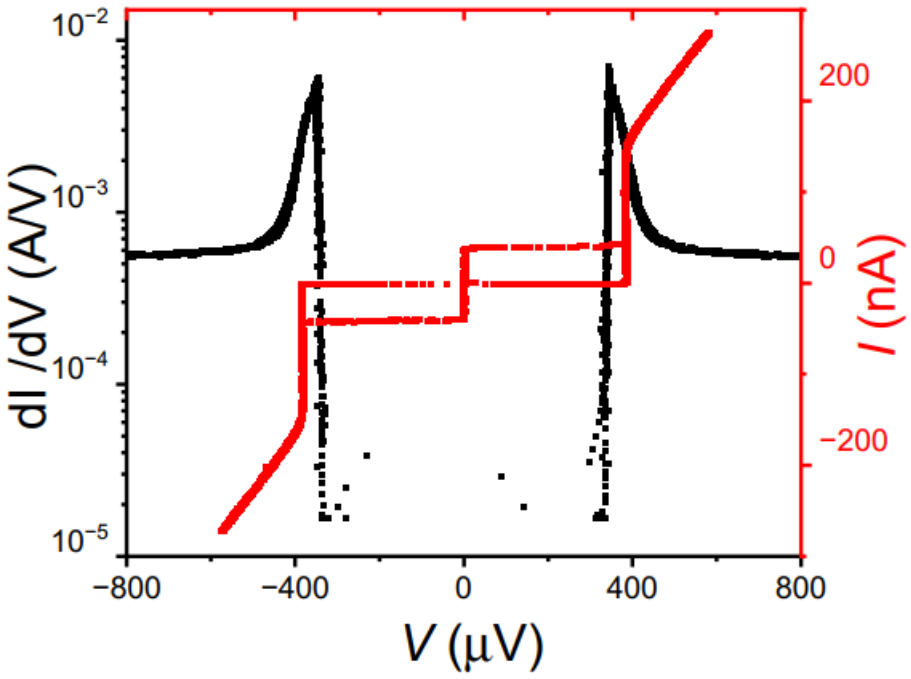

Figure 2.11: Graph representing the conductance measurement, superimposed on its current/voltage characteristic. Image of a SIS junction adapted from [18].

–3–
Device Fabrication

In this chapter I will collect all the information required to produce traditional multilayered JJs, including ferromagnetic layers and unconventional Van der Waals JJs, whose concepts and layouts could be of inspiration for novel generations of JJs.

3.1 Fabrication of JJs with Ferromagnetic Layers

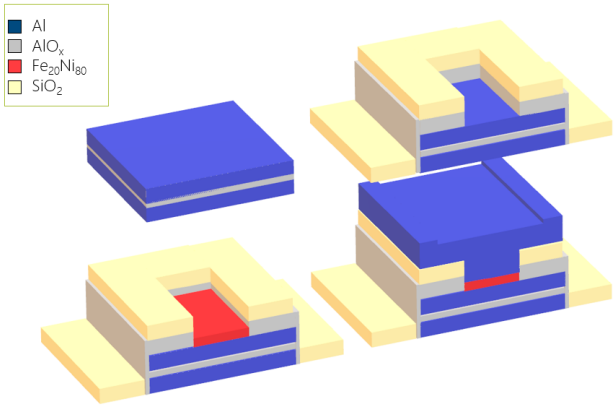

Figure 3.1: **Top-Left**: Deposition of three-layer of $Al - AlO_x - Al$. **Top-Right**: Process of Anodization and Insulation with SiO_2 and Al_2O_3. **Bottom-Left**: Deposition of Permalloy ($Fe_{20}N_{80}$). **Bottom-Right**: Deposition of Al wire contact [18].

In my thesis work, I have analyzed two chips containing ferromagnetic junctions with the same magnetic layer (Permalloy) and two different superconductors: Niobium and Aluminum. The ferromagnetic junctions were fabricated in collaboration between the University of Naples Federico II and the Institute of Applied Sciences e Intelligent Systems "E. Caianiello" ISASI-CNR at Pozzuoli, Naples (Italy).

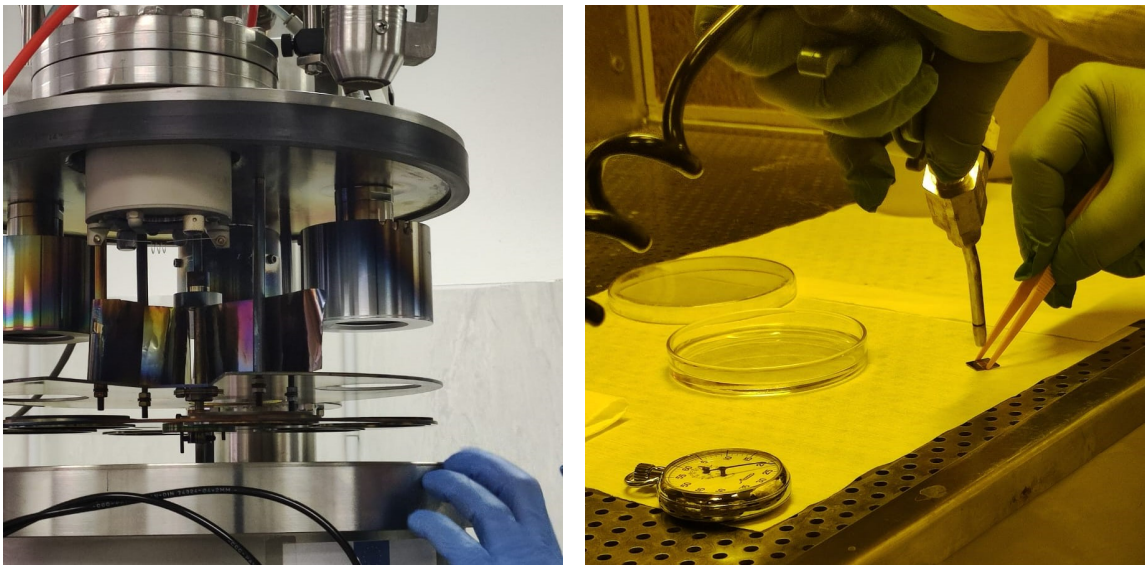

Figure 3.2: **Left**: Photo depicting the positioning of the chip inside one of the chambers of the rotating sputtering system at the CNR in Pozzuoli. **Right**: Chip development and cleaning after aluminum deposition.

The developed fabrication procedure useful for building the investigated JJs employing a ferromagnetic barrier, involves several fabrication steps. All the structures are made on a Si wafer covered by a SiO_2 layer $300nm$ thick. The substrate are cleaned using Acetone and Isopropanol solvents. Then in an ultra-high vacuum system ($\sim 3x10^{-8}Torr$), a Nb(Al)/AlO_x/Nb(Al) tri-layer is deposited (Fig. 3.1). The tri-layer is patterned using **Optical lithography**, which is a techniques that allows to transfer a pattern of suitable materials on a substrate. The wavelength of the light used determines the minimum size of features that can be formed in the light-sensitive chemical, known as photoresist, coated on the chip (in our case it is spin on the tri-layer). The resist undergoes chemical changes upon exposure to light, allowing for the selective removal of exposed regions by being developed using an appropriate chemical. The growth of materials is carried out by a **DC magnetron sputtering**, which involves emitting atoms from the surface of a target material due to collisions with ions from a gaseous plasma. The sputtering occurs within a high vacuum chamber (pressure below $10\mu Torr$) with the substrate and Nb(Al) target positioned facing each other, as in Fig 3.2. The tri-layer consists of a base electrode $\sim 200nm$ thick Nb/Al film, while the top electrode is made of a $\sim 40nm$ thick Nb(Al) film. Both electrodes are deposited at a rate of $0.8nm/s$. The intermediate Al layer, with a thickness of $\sim 7nm$, is deposited in situ at a lower rate of $0.7nm/s$. By filling the chamber with oxygen the Al layer forms an insulating barrier.

A selective anodization process is used to define the junction areas. This process defines the radius and therefore the air of the JJs. The dimensions of the junction areas used in this thesis work range from $\sim 25\mu m^2$ to $\sim 1\mu m^2$.

Consequently, the wafer is diced into $10x10mm^2$ chips, and Ar ion etching is employed to remove a $10nm$ layer of Nb/Al oxide before depositing the F layer. **Ion etching** (Ar^+), also known as plasma etching, is a process where the material is removed using plasma (highly ionized gas) instead of a liquid etchant. It offers higher selectivity and allows for finer control of the etching process, as depicted in Fig. 3.3. The Py layer, formed by

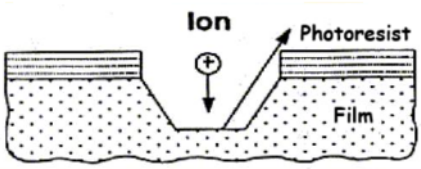

Figure 3.3: Etching processes using ions. The plasma generated by the ions during the bombardment of the surface allows for well-defined structures to be obtained.

$\sim 83\%Ni$ and $\sim 17\%Fe$ of thickness $\sim 3nm$, is then deposited using the lift-off technique. The Py material is sputtered by a DC magnetron sputtering source at a rate of $0.7nm/s$. Finally, $\sim 400nm$ thick top Nb/Al counter electrodes are deposited using DC sputtering and a lift-off process, completing the overall SIs'FS structure. Additional details on fabrication process are reported in [2].

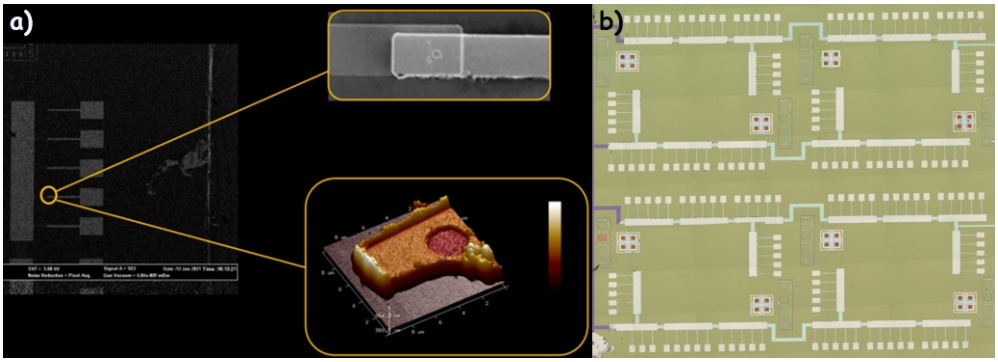

Figure 3.4: **a)** Image showing a junctions island, with zooms into the insets. Up: top -view of the Josephson junctions. Bottom: AFM of the circular junction, showing the junction area. **b)** The Optical image shows the developed design of the Superconducting Ferromagnetic Junctions.

The Fig. 3.4, shows the developed design of the Ferromagnetic Josephson Junctions chip that contain about 160 junctions. Specifically, as it is shown in Fig 3.4 a), each island contains a total of 5 junctions, with increasing transversal sizes (1 to 5 μm), called A, B, C, D, E. In total there are 32 islands, divided into 16 with circular geometry and 16 with square geometry. Each of these islands is bonded and then measured with 4-probe technique (appendix C) to probe the transport properties of each junction.

3.2 Fabrication of Tantalum Di-Sulfide JJs

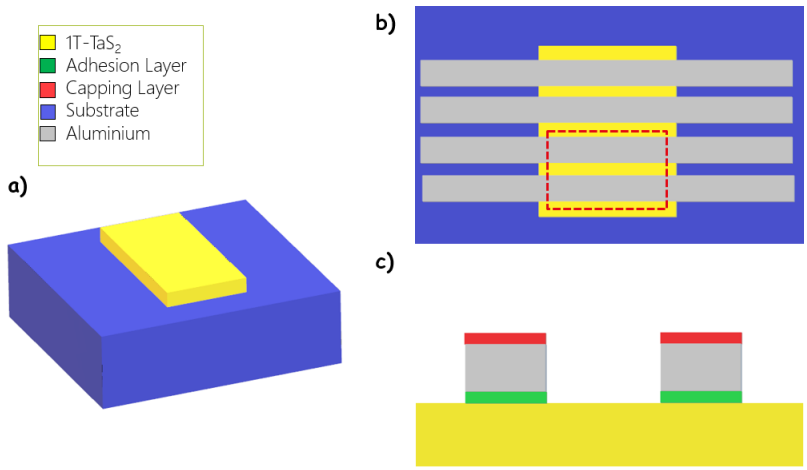

Figure 3.5: Sketch of the fabrication steps useful to make junctions based on 1T-TaS_2 flakes. **a)** 1T-TaS_2 flake is exfoliated and deposited on Si/SiO_2 substrate. **b)** top - view of the chip after EBL and aluminum deposition. **c)** cross - section of the red dotted part, highlighting the presence of an adhesion layer and a capping layer.

During my thesis I also collaborated on a project that involves the study of the properties of Josephson junctions with Van der Waals materials (1T-TaS_2), in collaboration with the university and the nano-fabrication center of excellence for nano-science and nanotechnology situated in Slovenia. The 1T-TaS_2 single crystals were synthesized using **Chemical vapor transport** (CVT) method. The details on the growth recipe are shown elsewhere [37]. The result of CVT growth are millimetre large high-quality crystals which have to be mechanically exfoliated in order to acquire thin films usually used for making devices. Fig. 3.5 shows an example of the developed design of both flakes and junctions.

Specifically, the chip is divided into an external part having pads for the gold electrical contacts, which begins in the outermost part of the chip with a width of hundreds of micrometers and then rejoin, decreasing their width, with a more internal part (blue in Fig. 3.6). The electrodes get closer to the flake, always decreasing their width, reaching a lateral size of hundreds of nanometers (Fig 3.6). The electrical contacts that ends on the flake are made of aluminium. In this way, the deposited electrodes run along the entire chip from the external pads to the innermost part, where the flake is positioned. In the innermost box the lithographic technique used, given the extremely small dimensions, is **Electron beam lithography (EBL)**, which is an advanced technique that utilizes a focused beam of electrons to write custom patterns onto a target material.

The design of the junctions (see Fig. 3.6) has been made by Klayout and the choice of gap e finger dimensions take into account the proximity effect of the EBL: back-scattered electron that affect the exposure of resist. A set of fingers $\approx 200nm$ wide and $\approx 1\ \mu m$ long have been designed and fabricated (Fig. 3.7) in order to overcome the proximity effect.

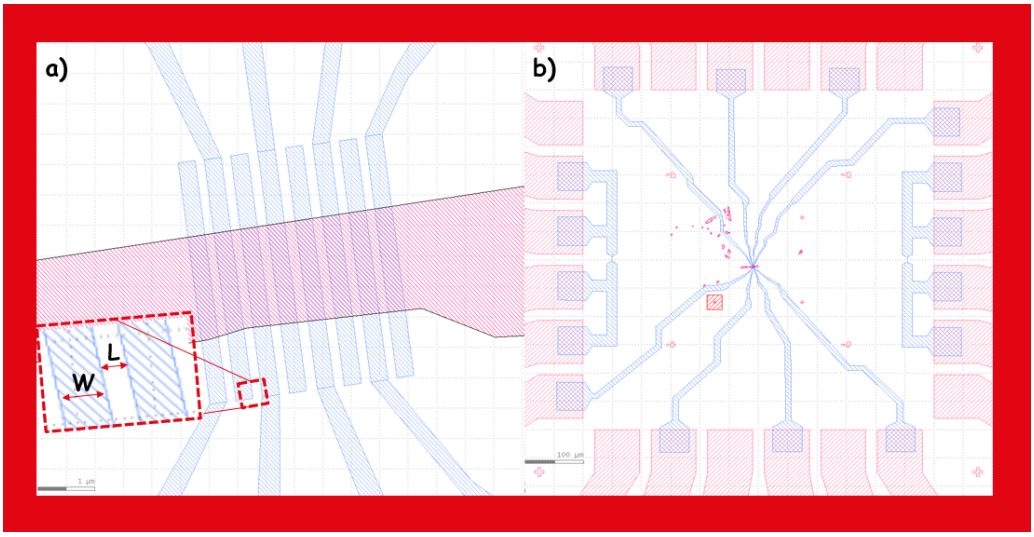

Figure 3.6: **a)** Computer Aid Design (CAD) with the tantalum di-sulfide flake (red) with the aluminum contacts (blue) an inset is also shown where the length between the electrodes $L \approx 100 - 200nm$ and the width of these $W \approx 200nm$ are shown. **b)** It shows the chip design.

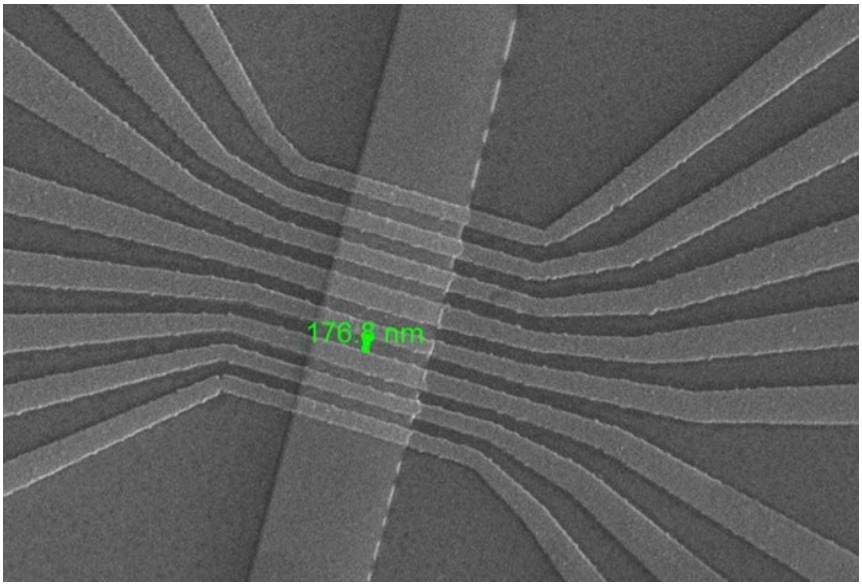

Figure 3.7: Scanning Electron Microscope(SEM) image of one of the firsts fabricated chips. The distance between two contacts is underlined in green, showing the length $L \approx 180nm$ of the gap.

These has been placed at a distance L that ranges from $\approx 100nm$ up to $\approx 200\ nm$. Due to the proximity effect the designed spacing L between the fingers differs (it is usually larger) from that made on chip. Several approaches have been used, in some cases also trying to have different distances between the gaps. To make the layout simpler, the number of fingers on each side has been reduced, allowing for more defined edges that are less affected by the fabrication processes relating to adjacent fingers.

The choice of L has to allow the overlap of the two superconducting wave functions inside the flake, so as to be able to induce superconductivity and therefore a current. In order to achieve the highest transparency at the interfaces between the 1T-TaS_2 flakes and the chosen superconducting materials, many tests have been carried out (we are currently working on it) whose goal is to find an inter-layer useful to improve the matching of the Fermi levels between the coupled materials and improve their adhesion. Three different set of JJs having different Adhesion layer were made (Cr, Pd, Ti), its thickness has been fixed to $7nm$. All the junctions have been characterized at lowest temperature and the results are discussed in the chapter 5.

3.3 Chip Wiring and Bonding

The magneto-transport properties of the devices characterized in this thesis required to be electrically connected to the setup of measure. Pads (Fig. 3.9) having the size of hundreds micrometer squared have been linked to an Al wire whose diameter is of the order of tens micrometers via a tool called bonding machine. The used bonder Fig 3.8 is from the K&S 4500 Series Manual Wire Bonders, which are specialized equipment used for wire bonding applications. As a matter of fact they provide precise control over bonding parameters, such as bonding force, ultrasonic energy, and bonding time. These parameters can be adjusted based on the specific requirements of the device being bonded.

To apply a bond on a chip between two pads, a manual or semi-automatic procedure is performed (Fig. 3.8). A tip containing a thread of the material to create the connection slowly descends towards the desired area, then thanks to the use of an ultrasound signal, the material (Aluminum) is welded with one of the two pads. To obtain an optimal weld a careful choice of parameters is necessary, such as time and signal amplitude. After having made the first bond the tip rises to an intermediate height to allow the application of the second bond, which following the example would be concluded on the chip. Fig. 3.9 shows the chip holder fabricated and characterized in this thesis, connected to the chip through aluminum wires. It is interesting to note that there are asymmetric structures on the chips that allow orientation during the bonding operation.

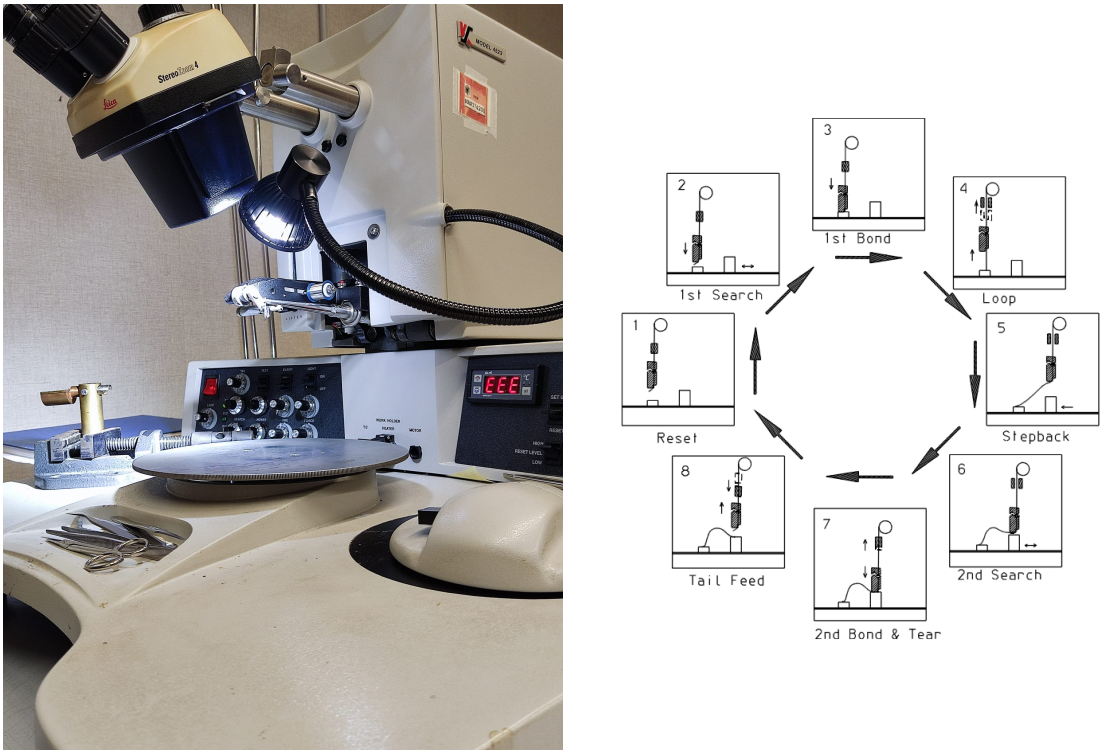

Figure 3.8: **Left**: K&S 4523 Wire Bonder Model. **Right**: Wedge Bonding Cycle in Semi/Automatic Mode - 90° Wire Feed [38].

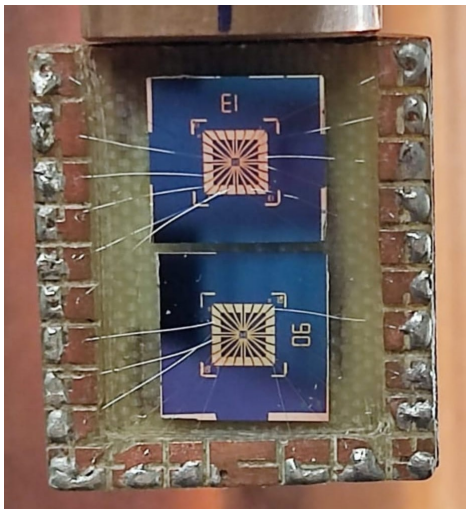

Figure 3.9: Aluminum Bonds performed on Tantalum Di-Sulfide Chips placed on a chip holder with the K&S 4523 Wire Bonder.

–4–
Ferromagnetic Josephson Junctions

In this chapter a comparison will be made between the DC transport properties at low temperatures of the ferromagnetic Josephson junctions (JJs) fabricated with Niobium and Aluminum. The investigation of the made JJs is carried out by comparing their transport properties by recording the current-voltage characteristics[39, 40], as well as the behavior in the magnetic field[41, 42, 43] and the differential conductance [18]. Some of the just mentioned measurements have been done also changing the temperature.

The studied JJs represent a possible circuit element for quantum computation [44, 45], cryogenic memories [39, 46], single-photon detectors and spintronics [33, 47]. The fabrication of these junctions has already been described in chapter 3, here we limit ourselves to analyzing the transport properties at base temperature, as the temperature varies and the behavior in a uniform magnetic field.

4.1 Tunnel junction SIS: Aluminum ad Niobium

Current-Voltage curves as a function of the temperature have been measured for tunnel junctions (SIS) that could serve as a reference junction for junctions based on Al and Nb employing a thin Permalloy (Py) ferromagnetic layer. Tunnel junctions consist of Al(200 nm) - AlOx(3 nm) - Al(400 nm) or Nb(200 nm) - AlO_x(3 nm) - Nb(400 nm) while those employing a thin ferromagnetic layer will form an SIs'FS JJ. In this sub-section the transport properties of the tunnel reference junctions made by Al and Nb superconductive contacts will be discussed. These comparative measurements help to better focus the peculiar features of those employing F layers. Current - Voltage curves are measured by using the experimental setup shown in section 2.2. At the temp $T = 10\ mK$ a current voltage curve is shown in Fig. 4.1, that reveals four distinct regions :

1. **The superconducting segment**, depicted by the branch where a finite current flows while the voltage (V) remains at zero. The beginning and end of this vertical line are marked by a precise current value, called the critical current (I_c).

2. **The switching segment**, which corresponds to the transition from the supercon-

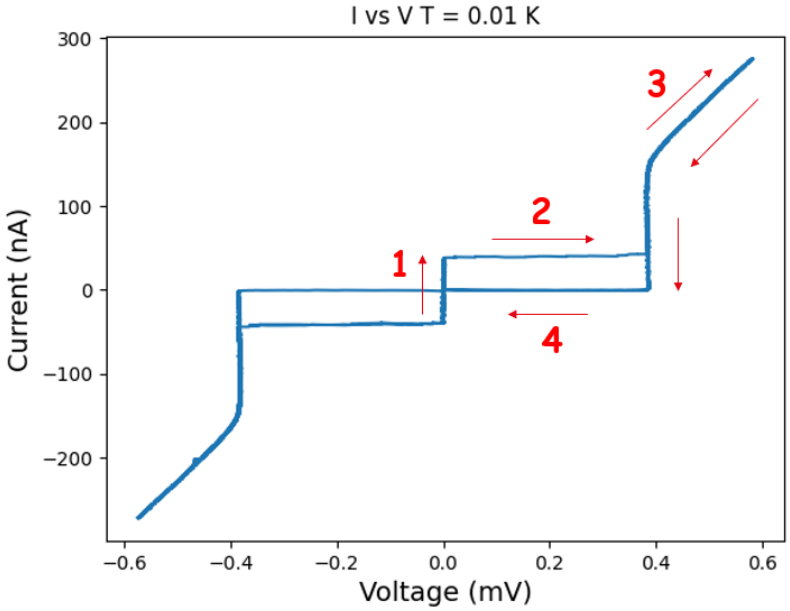

Figure 4.1: Current - Voltage characteristic for a circular ($R = 2\ \mu m$) SIS Josephson junction, based on a Aluminum technology, for a SIS type: Al(200 nm) - AlO_x(3 nm) - Al(400 nm).

ducting ($V = 0$) to the ohmic arm.

3. **The ohmic region**, where the characteristic displays a linear behavior, allowing for the extrapolation of the normal resistance (R_n) of the junction.

4. **The re-trapping segment**, is the responsable of the hysteresis behaviour of the JJ and its physical meaning has been discussed in section 1.2.

By changing the temperature as described in chapter 2, the current-voltage curves for each temperature are measured. Fig. 4.2 shows all the curves measured for Al - AlO_x - Al and Nb - AlO_x - Nb junctions. SIS based on Al electrodes shows a critical current value I_c equal to 39 ± 2 nA and a normal resistance R_n of the order of 1700 ± 34 Ω, while the Niobium based JJ has an I_c of 20.0 ± 1 μA and R_n of 74 ± 2 Ω.

From the curves in Fig. 4.2 fixing a threshold in voltage of the order of a few hundred μeV for both positive and negative arm, the critical current I_c has been estimated for each temperature as it has been shown in Fig. 4.3. The normal resistance is obtained by performing a linear fit of the current-voltage curve for absolute voltage values higher than those of the gap (Al gap ≈ μeV; Nb gap ≈ meV).

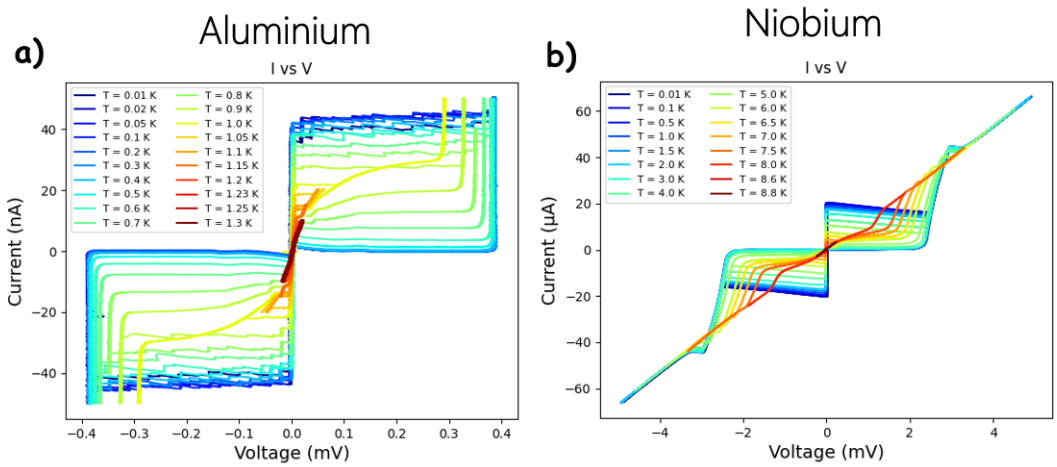

Figure 4.2: Current-Voltage as a function of in relation to temperature changes for a circular Josephson junction ($R = 2\ \mu m$) comprised of **a)** Al(200 nm) - AlO_x(3 nm) - Al(400 nm).**b)** comprised of Nb(200 nm) - AlO_x(3 nm) - Nb(400 nm).

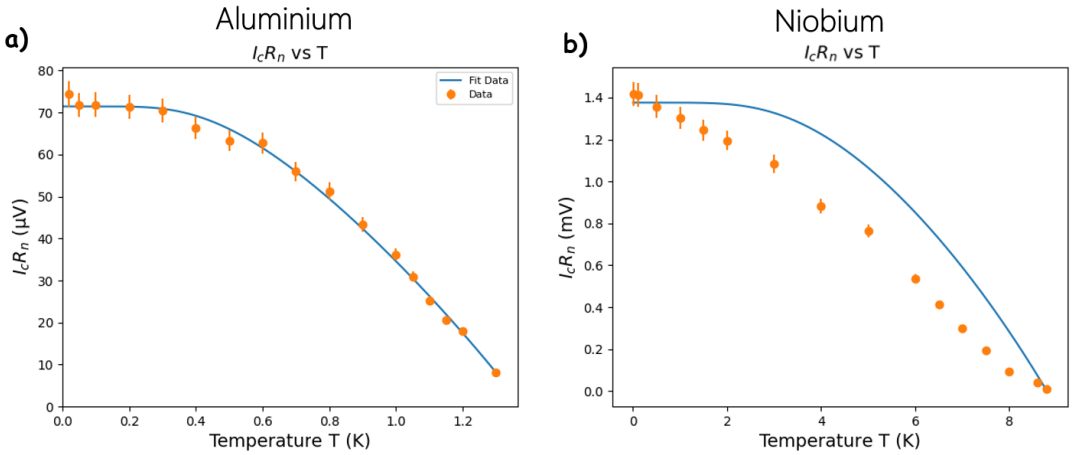

Figure 4.3: I_cR_n product vs T for a SIS junction made with Aluminum and in blue the Ambegaokar- Baratoff curve. The investigation has been carried out for a circular (R = 2 μm) **a)** Al(200 nm) - AlO_x(3 nm) - Al(400 nm) junction. **b)** Nb(200 nm) - AlO_x(3 nm) - Nb(400 nm) junction.

As already described in chapter 1, the product of the critical current I_c by the normal resistance R_n represents the voltage drop across the device and its temperature trend can allow to estimate fundamental characteristics, such as the superconducting gap. Therefore the latter can be compared with the value experimentally obtained from the conductance. In Fig. 4.3 I_cR_n temperature behaviour is plotted as a function of the temperature simultaneously with an Ambegaokar-Baratoff (Eq 4.1) curve, which predicts

the I_cR_n values in the case of an ideal tunnel junctions.

$$I_cR_n(T) = A\frac{\pi}{2}\frac{\Delta(T)}{e}\tanh\left(\frac{\Delta(T)}{2k_BT}\right) \tag{4.1}$$

where Δ follows Eq. 1.6, T is the temp, k_b Boltzmann constant and A is a suppression factor. For Aluminium $A = 0.29$, $\Delta_0 = 0.16\ meV$ and $Tc = 1.3K$, while for Niobium $A = 0.73$, $\Delta_0 = 1.20\ meV$ and $T_c = 8.8K$. For Aluminium $I_cR_n = 74 \pm 3\ \mu V$ at the lowest temperature, while for Niobium $I_cR_n = 1.4 \pm 0.1\ mV$. The estimated values are the following listed, and shows how the JJs made with Al, better than Nb based JJs, approximate the ideal tunnel JJs. Even their I_cR_n product are quite closer to the superconducting gap of the invested JJs, thus confirming their high quality.

As already described previously in chapter 2, conductance measurements provide an additional measure for the analysis of the transport properties of the junction, showing a direct measure of the superconducting gap and R_n.

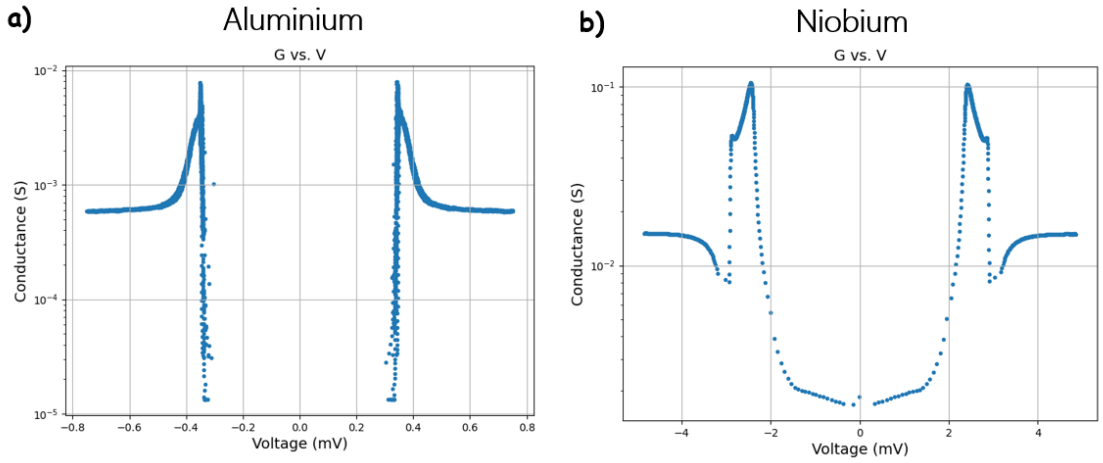

Figure 4.4: Conductance $\frac{dI}{dV}$ measurement in log scale for the SIS junction with radius of R = 2 μm: **a)** shows Al(200 nm) - AlO_x(3 nm) - Al(400 nm) $T = 10\ mK$ while Fig. **b)** Nb(200 nm) - AlO_x(3 nm) - Nb(400 nm) at $T = 10\ mK$.

In the Aluminum case (Fig. 4.4) there are no particular features, showing a vertical sub-gap zone and a conductance value of $Rn = 1699 \pm 34\ \Omega$ compatible with the resistance value estimated in the linear fits. The value of the superconducting gap is estimated as $\Delta = 0.1700 \pm 0.003\ meV$, compatible with that achieved by the A.B. fit. Differently from the Niobium case the sub-gap presents a slight curve compared to the case of aluminum, showing a presence of quasi-particles, which is responsible for the dissipation mechanisms thus hampering its employing in circuits for quantum computation. For the Nb it has been estimate, from the conductance measurements, a superconducting gap of $\Delta = 1.200 \pm 0.003$ meV and a normal resistance of $R_n = 66 \pm 1\ \Omega$.

4.1.1 Magnetic Properties

As already analyzed in chapter 1, a Josephson junction immersed in a magnetic field shows a modulation of the critical current which is reflected in a variation of the current-voltage curve. The system used for this type of measurement has already been described in chapter 2. Fig. 4.5 shows the magnetic transport curves for the two tunnel junctions.

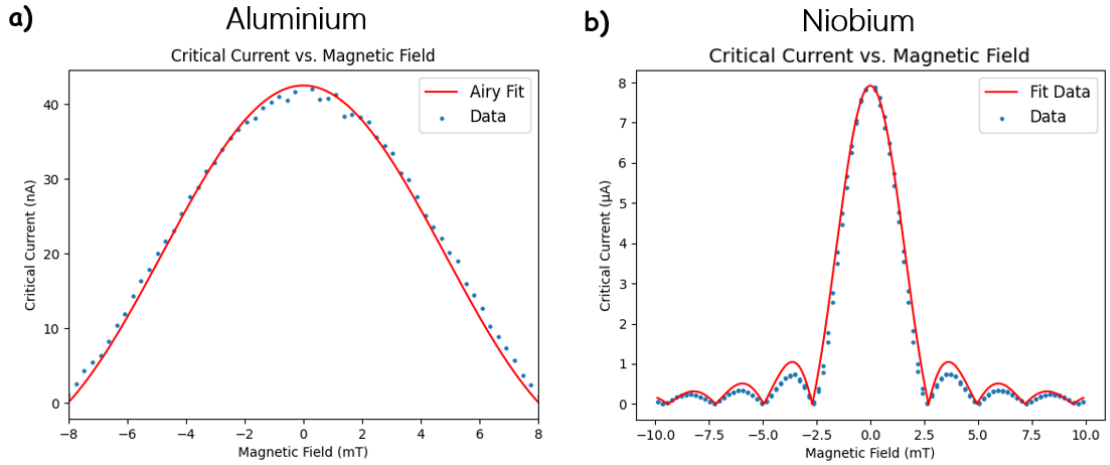

Figure 4.5: The scattered points depict the empirical data of the $Ic(H)$ for a circular SIS Josephson junction that consists of: **a)**Al(200 nm) - AlO_x(3 nm) - Al(400 nm), with a radius of R = 2 μm. **b)** Nb(200 nm) - AlO_x(3 nm) - Nb(400 nm), with a radius of R = 2 μm. In red the fit curve of the Airy model (see relation in chapter 1).

Since the junction is circular, we expect an Airy pattern [25], from which it is possible, knowing quantities such as the thicknesses and radius of the junction, to obtain the λ_L (section 1.3) that in the Aluminum case $\lambda = 38 \pm 1$ nm while for the Niobium $\lambda = 115 \pm 2$ nm. These values are in agreement with those found in literature and summarized in Table 1.2.

4.2 Ferromagnetic JJs SIsFS: Aluminum and Niobium

In this thesis I have also investigated the magneto - transport properties of JJs employing an unconventional Josephson Junctions with ferromagnetic layer of Py. These junctions have a stacked layout and are based on two different superconductors: Al and Nb. Their structure is made by the following layers: Al(200 nm) - AlO_x(3 nm) - Al(30 nm) - Py (30 nm) - Al(400 nm) and Nb(200 nm) - AlO_x(3 nm) - Nb(30 nm) - Py(3 nm) - Nb(400 nm). The presence of the ferromagnetic layer within the junction is expected to change the magneto-transport properties, both in the case of aluminum and in the case of niobium.

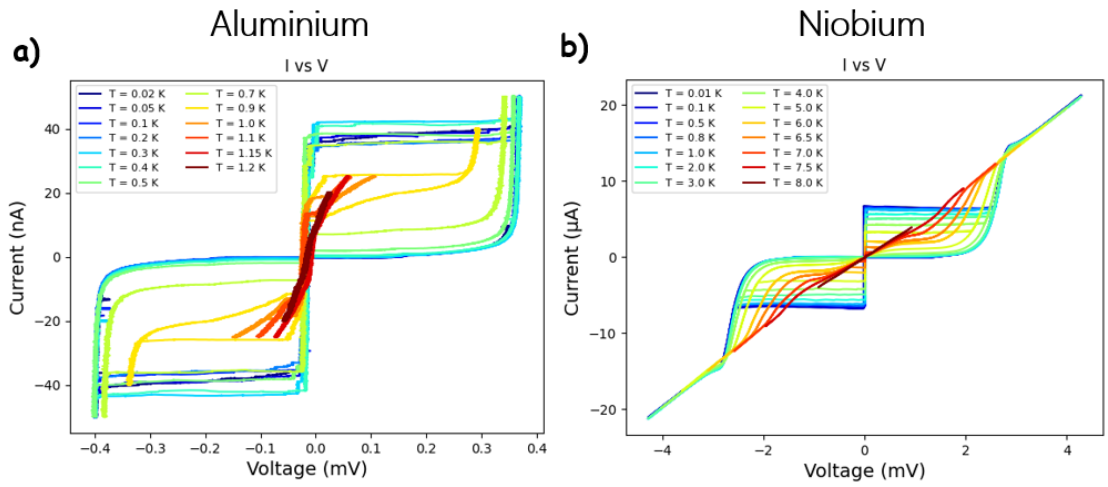

Figure 4.6: Current-Voltage characteristics as a function of the temperature changes for a circular JJ having the radius $R = 2\mu m$: **a)** Al(200nm) - AlO_x(3nm) - Al(30 nm) - Py(3 nm) - Al(400 nm) and **b)** Nb(200 nm) - AlO_x(3 nm) - Nb(30 nm) - Py(3 nm) - Nb(400 nm).

4.2.1 Transport Properties

The transport properties of the SIs'FS junction have been investigated. The Current - Voltage curves are reported in Fig. 4.6 and show all the measured I-V for the SIs'FS junctions based on Al and Nb. At the lowest temperature the Aluminum SIs'FS junction shows $I_c = 41 \pm 2\ nA$ and $R_n = 1792 \pm 36\ \Omega$, while the critical current value for ferromagnetic junction based on Niobium is $I_c = 20.0 \pm 1\ \mu A$ and the normal resistance is $R_n = 200 \pm 4\ \Omega$. A worthy consideration lies in the determination of the critical current value, which emerges as nearly indistinguishable from the SIS case. This observation provides a compelling indication that the supercurrent within this junction remains unimpeded, irrespective of the constituent layers or the multiple barriers interposed between them. This outcome underscores the quality of the fabrication process.

4.2.2 IcRn as a Function of the Temperature

Fig. 4.7, on the left for Al, on the right for the Nb shows the I_cR_n plot for the two investigated junctions. Here the data are compared to the Ambegaokar-Baratoff (A.B) prediction. Former comparison between the experimental data and the theoretical one for Al based JJs and the Nb based one, shows that the Al has a minor discrepancy from theoretical curve. The estimated parameters obtained for the Aluminum JJs are $I_cR_n = 74 \pm 3\ \mu V$, while $A = 0.25$, $\Delta_0 = 0.19\ meV$ and a $Tc = 1.2\ K$ for the A.B. trend. Nb based JJs show $I_cR_n = 1.300 \pm 0.05\ mV$ and in Fig. 4.7 the curve depicted has the following parameters: $A = 0.73$, $\Delta_0 = 1.2\ meV$ and a $Tc = 8K$.

Fig. 4.7 shows, as well as the Nb tunnel junction, that I_cR_n curve does not follow the A.B. trend. It can be interpreted as an achieved lower quality of the tunnel barrier of the

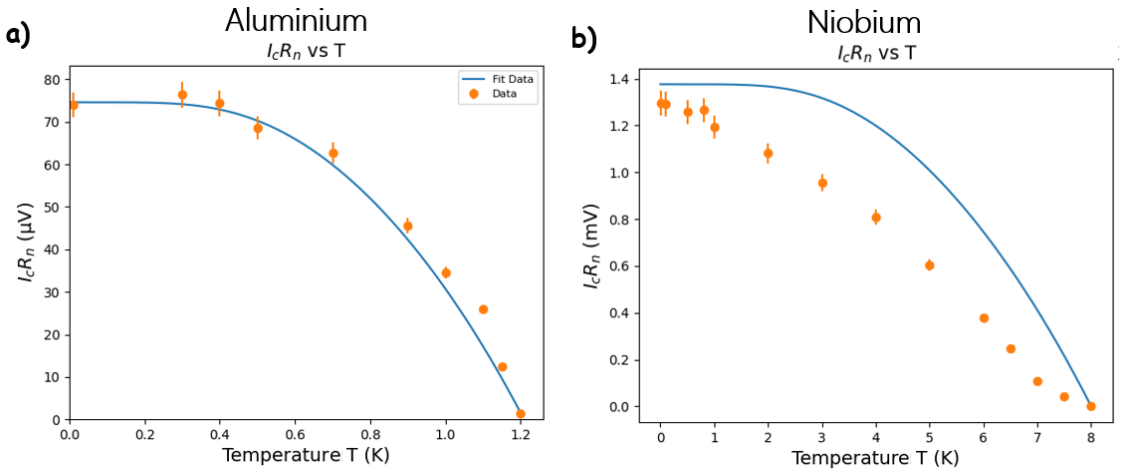

Figure 4.7: I_cR_n product vs T for a SIsFS junction made with Aluminum (Niobium) and in blue the Ambegaokar-Baratoff fit (curve). The investigation has been carried out for a circular R=2 μm **a)** Al(200 nm) - AlO_x(3 nm) - Al'(30 nm) - Py(3 nm) - Al(400 nm) junction. **b)** Nb(200 nm) - AlO_x(3 nm) - Nb(30 nm) - Py(3 nm) - Nb(400 nm).

Nb based JJs than in the Al JJs. It could be due to a higher intrinsic roughness on Nb surface than hampers the uniform growth of the AlO_x insulating layer, thus allowing the pin-holes to work like superconducting channels that circumvents the tunnel effect of the barrier.

4.2.3 Conductance and Magnetic Measurements

Fig. 4.8 displays the conductance measurements, they have been even carried out for JJs employing a thin ferromagnetic layer. By comparing it with those of Fig. 4.4 (measured for SIS JJs) is clearly shown a different shape with extra figures due to the multilayered layout where quasi-particles can be the responsible of the dissipative effects. The investigated ferromagnetic junctions based on the Al show a dissipation due to quasi-particles. Former values are $\Delta_0 = 0.180 \pm 0.004\ meV$ and $R_n = 1793 \pm 36\ \Omega$ for Aluminum, in remarkable agreement with that extrapolated from a different kind of measurement (current-voltage). The same analysis has been carried out on Niobium based ferromagnetic junctions and it shows $\Delta_0 = 1.30 \pm 0.03\ meV$ and $R_n = 199 \pm 4\ \Omega$.

Here too, the properties of the junction were measured by varying the applied magnetic field. In order to realize a magnetic switching device with hysteretic behavior of the critical current, it is crucial that $d_s < \lambda_L$ [48, 35]. From the Aluminum SIS the Al London penetration depth we have estimated $\lambda_L \approx 40\ nm > d_s$, and for Niobium $\lambda_L \approx 115\ nm > d_s$. Therefore, a hysteretic behavior of the $I_c(H)$ is expected.

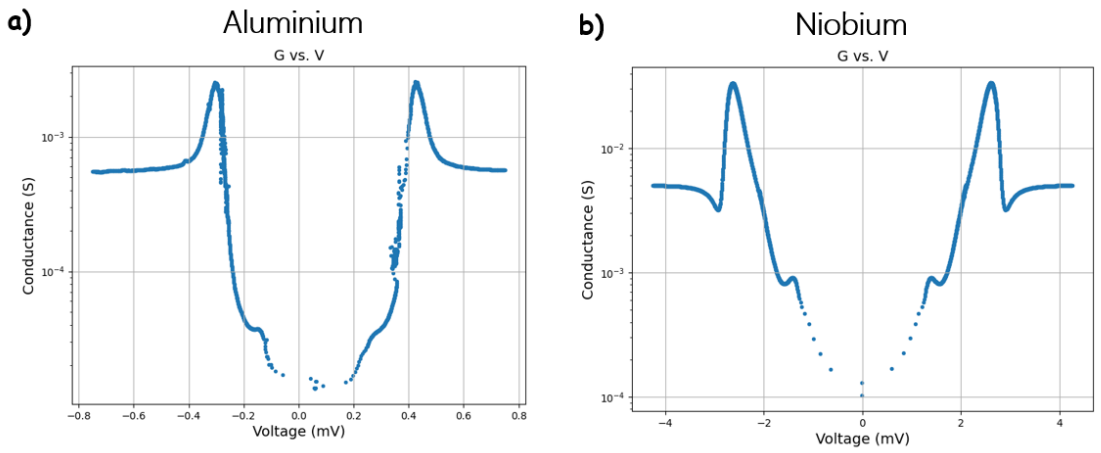

Figure 4.8: Conductance $\frac{dI}{dV}$ measurement in log scale for the SIsFS junctions with radius of R = 2 μm. Fig **a)** shows Al(200 nm) - AlO_x(3 nm) - Al'(30 nm) - Py(3 nm) - Al(400 nm) while **b)** Nb(200 nm) - AlO_x(3 nm) - Nb(30 nm) - Py(3 nm) - Nb(400 nm) junctions.

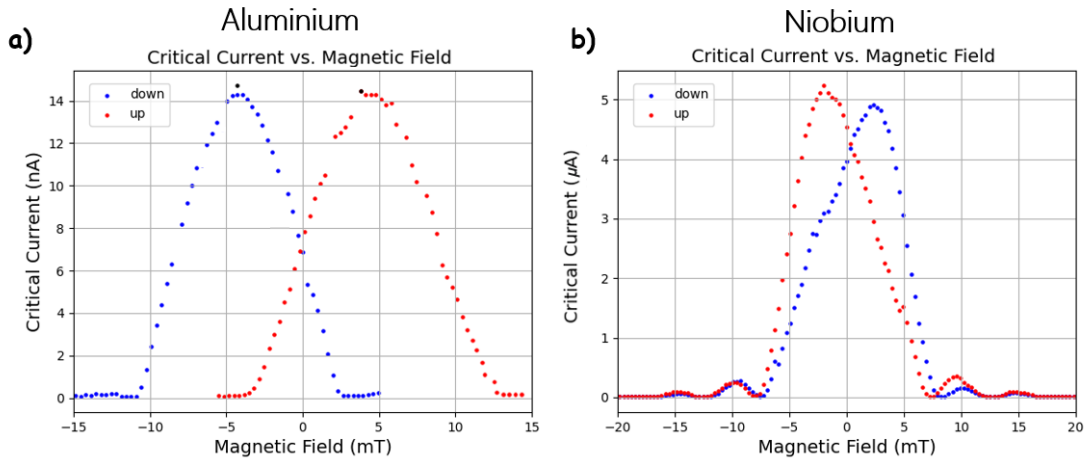

Figure 4.9: The scattered points depict the experimental data of the $I_c(H)$ behavior for a circular Josephson junction of the SIsFS configuration: **a)** Al(200 nm) - AlO_x(3 nm) - Al'(30 nm) - Py(3 nm) - Al(400 nm) **b)** Nb(200 nm) - AlO_x(3 nm) - Nb(30 nm) - Py(3 nm) - Nb(400 nm), with a radius of R = 2 μm.

The Niobium junction has shown a new intriguing feature as shown in Fig 4.9 on the right. It can be observed an inverse hysteresis of the $I_c(H)$ curves, i.e., a shift of the $Ic(H)$ curves in the opposite direction to the one due to magnetization (section 1.3). For instance, the maximum of the down curves at a positive field H_d and the maximum of the up curves at a negative field H_u. While the well-established phenomenon of the superconducting order penetrating into a ferromagnetic material, known as the proximity effect, is widely recognized, we have encountered an unconventional phenomenon in this

Table 4.1: Experimental Results

JJs	$I_c(nA)$	$R_N(k\Omega)$	$I_cR_N(\mu V)$	$J(\frac{mA}{cm^2})$	$E_J(\mu eV)$
SIS (Al)	39 ± 2	1.70 ± 0.03	74 ± 3	310 ± 31	160 ± 3
SIsFS (Al)	41 ± 2	1.79 ± 0.04	74 ± 3	330 ± 32	180 ± 4
JJs	$I_c(\mu A)$	$R_N(\Omega)$	$I_cR_N(mV)$	$J(\frac{A}{cm^2})$	$E_J(meV)$
SIS (Nb)	20 ± 1	74 ± 2	1.4 ± 0.1	159 ± 10	1.20 ± 0.03
SIsFS (Nb 10)	0.100 ± 0.002	440 ± 9	1.4 ± 0.1	3.1 ± 0.3	0.70 ± 0.01
SIsFS (Nb 30)	20.0 ± 0.4	200 ± 4	1.3 ± 0.1	159 ± 10	1.30 ± 0.03

case. This phenomenon is the inverse proximity effect, where the ferromagnetic order leaks into a superconductor from the interface between the two materials. To elaborate, electrons within Cooper pairs that have their spins aligned with the exchange field and it relatively easy to enter the ferromagnetic (F) layer. Conversely, electrons with spins oriented in the opposite direction tend to remain within the superconducting (S) layer. Consequently, the surface of the superconducting layer takes on a net magnetization with a direction opposite to that of the ferromagnetic material. This effect may even compensate for the magnetic moment of the ferromagnetic material, thus resulting in a reduction, or even a completely absence, of the magnetic shift. The shift value estimated is approximately equal to $H_u = 3.80\ mT$ and $H_d = -4.29\ mT$ for Aluminum, while for Niobium it's $H_u = -2\ mT$ and $H_d = 2.31\ mT$. The shift, present in different measures for both junctions analyzed, allows us to conclude that these junctions have a well-defined magnetic behavior. Their sensitivity to the magnetic field, maintaining a behavior very similar to conventional SIS junction, is a very important experimental result, especially from an application point of view.

4.3 Nb Based JJs employing the s' 10 nm thick

Ferromagnetic junction based on Nb electrodes having a thinner (10 *nm* thick) s' layer have been also studied. Their structure is: Nb(200 *nm*) - AlO_x(3 *nm*) - Nb(10) - Py(3 *nm*) - Nb(400 *nm*). The different thickness of s' layer drives the multi-structured layered junction into regime of a single junction [35]. In this configuration, the supercurrent can be suppressed within the s' inter-layer, as theoretically predicted by the theoretical model discussed in Chapter 1, Sec 1.4. In Fig. 4.10 the Current - Voltage curves as a function of the temperature are displayed for the junction having as radius $R = 1 \pm 0.1\ \mu m$. The critical current value is $I_c = 10 \pm 0.4\ nA$ while for normal resistance we get $R_n = 440 \pm 10\ \Omega$. Also in this case the estimates of critical current and normal resistance were measured in the range of temperature from the base one up to the critical one, which in this case turns out to be nearly $\approx 5\ K$. The reason why the critical temperature differs significantly from that found previously is related to the thickness of the superconductor between the insulator and the ferromagnetic part. The thickness chosen in this case does not favor the complete construction of a superconducting gap, which is lower in comparison to the one

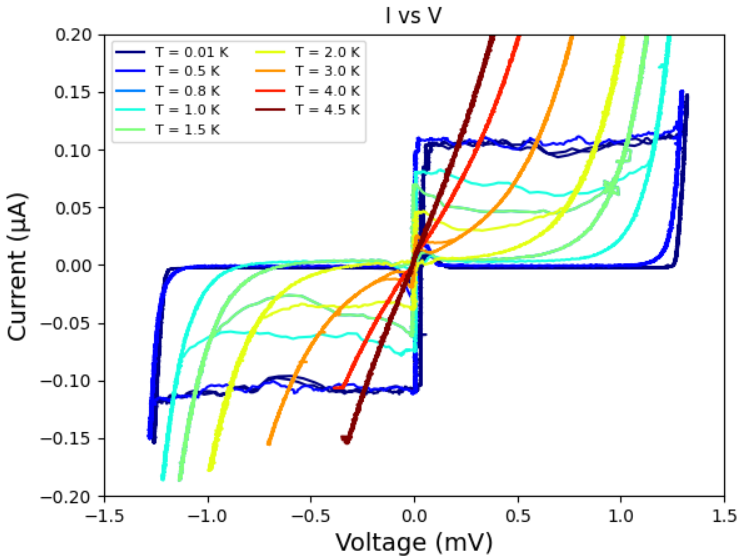

Figure 4.10: Current-Voltage relationship as a function of the temperature for a circular Josephson junction ($R = 1\ \mu m$) made of Nb(200 nm) - AlO_x(3 nm) - Nb(10 nm) - Py(3 nm) - Nb(400 nm).

of the bulk superconducting electrodes, thus leads the transport into that of the proximity driven effect [35]. The consequences can be appreciated from the trend of the I_cR_n product in temperature shown in Fig. 4.11. The conductance measurements carried out (Fig. 4.12) show a transport with a reduced superconducting gap, $\Delta_0 = 0.74 \pm 0.02\ meV$, while for the normal resistance, accordingly to the I-V measurements is $R_n = 465 \pm 10\ \Omega$. The reduced gap is compatible with the reduced critical temperature within BCS theory and with nano-fabrication.

While for conducting magnetic measurements on this junction (Fig. 4.12), we did not observe the expected hysteresis behavior in $I_c(H)$. Similar to what was observed in the Niobium junction with $d_s \approx 30\ nm$, this lack of hysteresis may be attributed to the presence of the inverse proximity effect. In such cases, the net magnetization of the ferromagnetic layer could be entirely suppressed, resulting in a complete absence of a shift in the pattern.

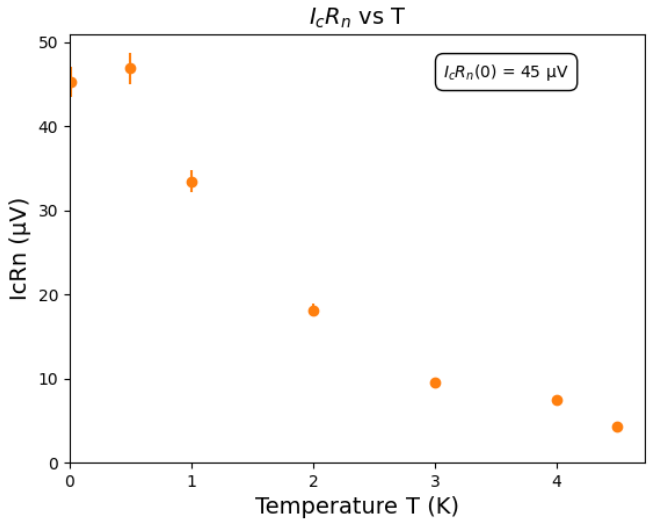

Figure 4.11: I_cR_n product vs T for a circular SIsFS Nb(200 nm) - AlO_x(3 nm) - Nb(10 nm) - Py(3 nm) - Nb(400 nm) junction made with Niobium that has (R=1 μm).

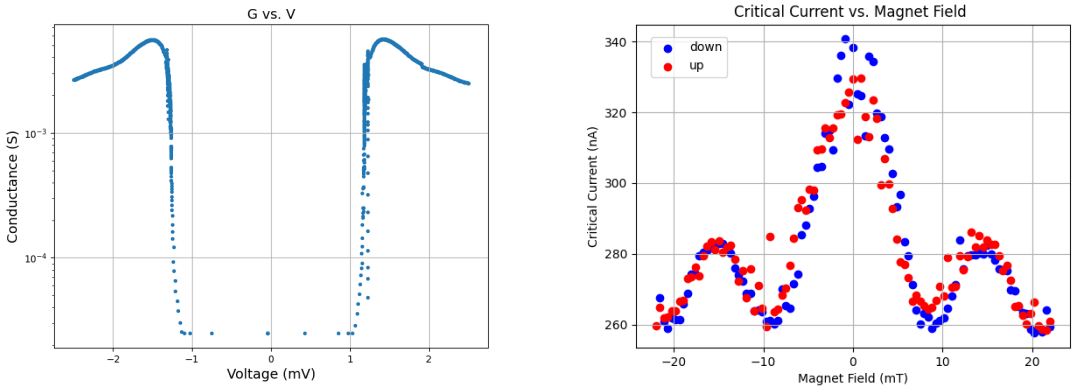

Figure 4.12: **L)** Conductance $\frac{dI}{dV}$ vs voltage curve in log scale for the SIsFS Nb(200 nm) - AlO_x(3 nm) - Nb(10 nm) - Py(3 nm) - Nb(400 nm) junction with radius of R = 1 μm at T = 10 mK. **R)** The scattered points show the experimental data of the $Ic(H)$ curve for a R = 1 μm circular Josephson junction of the SIsFS Nb(200 nm) - AlO_x(3 nm) - Nb(10 nm) - Py(3 nm) - Nb(400 nm).

–5–
Josephson Junctions Employing 1T-TaS_2 Flakes

In this chapter I will discuss the embrional results on the projects where flakes of van der Waals materials (1T-TaS_2) represent the building block of junctions based on Al superconducting reservoirs. The project, currently under development, is made in collaboration with the group of Prof. Dragan D. Mihailovic of the Jozef Stefan Institute at the University of Ljubljana (Slovenia). It will be investigated the magneto-transport properties as a function of the temperature and of the electric nano pulses. Few attempts to induce the superconducting properties into the flake have also been made and it will be discussed, but this challenging and interesting aspect is currently under investigation.

5.1 Material and Applications

1T-TaS_2 is a crystalline material belonging to the family of tantalum di-chalcogenides [49]. It behaves like a two-dimensional (2D) Van der Waals material that has been studied for its interesting electronic properties [50]. The notation "1T" refers to the crystal structure of the material, which has a hexagonal (trigonal) electronic phase transition layer it has been shown in Fig 5.1. Due to its intriguing electronic properties [51], 1T-TaS_2 has been researched for potential applications in advanced electronic devices, such as transistors, memories, and other electronic switching technologies [52]. The phase diagram of 1T-TaS_2 [53], displays a wide array of phenomena such as different charge-density-wave (CDW) states, Mott transitions [54], polaronic ordering [49, 55], and even superconductivity under higher pressures [56]. At temperatures above 540 K [37], the material exhibits typical metallic behavior. When cooled further, it undergoes a phase transition into different CDW states. Upon slow cooling below $160 - 180K$ the material becomes a Mott insulator with a gap of $0.1eV$ [4]. This results in a sudden jump in electrical resistance at approximately $160K$ [57], which further increases as the temperature decreases to around $20K$. Notably, temperatures around $20K$ or lower are commonly used in devices based on Charge Configurable Memory (CCM) materials. From $20K$ to room temperature, the

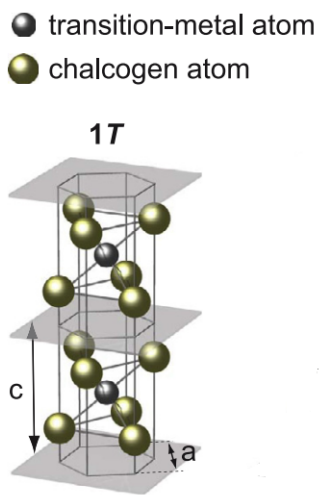

Figure 5.1: It shows the crystal structure of 1T-TaS_2 type. Adapted from [4].

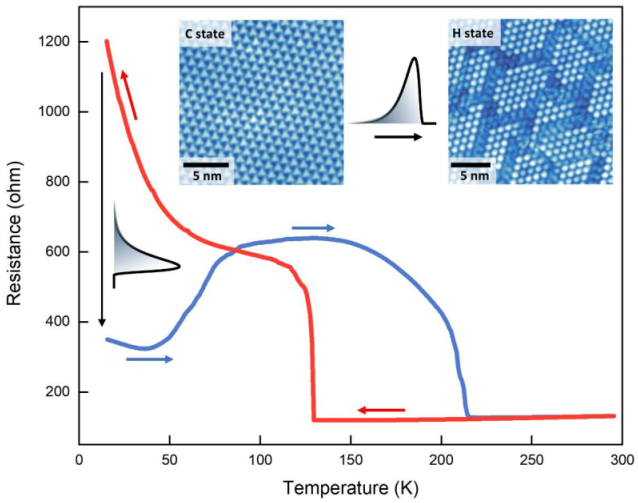

Figure 5.2: The electrical resistance of the 1T-TaS_2 flake decreases upon cooling (red curve), and then a single 1.9ps electrical pulse at 16K induces resistance switching of the flake (black arrow). The scanning tunneling microscope (SEM) images of the C state (left inset) and the H state (right inset) are provided for illustration, showing the charge reordering involved in the switching process [52].

resistance curve follows a hysteresis loop, indicating complex phase transitions. Outside of the normal phase transitions, others transition of a different nature are currently under investigation, which are crucial for a particular type of device called Charge Configuration Memory (CCM). CCM devices utilize the reconfiguration of electronic domains between the ground state and an excited one, in this specific case, the recently discovered metastable **hidden (H) state** in the layered transition metal dichalcogenide (TMD) 1T-TaS_2 crystal [58]. The device's electrical resistance undergoes a significant change as it switches between these different electronic states [37], as shown in Fig. 5.2.

5.2 Induced Superconductivity

As it has been discussed in the first chapter, when two superconducting banks are coupled to a normal material, the properties of the materials and the contact transparency play the main role in the junctions transport properties. The contact's transparency between superconducting reservoirs works like a knob thus tuning the superconducting properties of the entire junction [59]. For example, high achieved transparency in junctions based on flakes of graphene enables a critical current to pass through a micrometer long graphene [28], while InAs nanowire coupled to Al electrodes have shown different critical current amplitude even having quite close contact transparency [60]. The phenomena that allows to drive the behaviour of the hybrid junctions (superconductor-normal-superconductor) towards the superconducting phase is sometimes referred to as an induced gap and it appears because of the proximity effect [22, 23, 25]. For innovative class of materials, this proximity induced gap can drive a transition into a topological phase where its excitations obey non–abelian statistics and have been proposed as qubits in fault–tolerant topological quantum computing schemes [61, 62]. Last few years, several very encouraging reports on the experimental signatures of Majorana excitations have appeared [63, 64]. In our study,

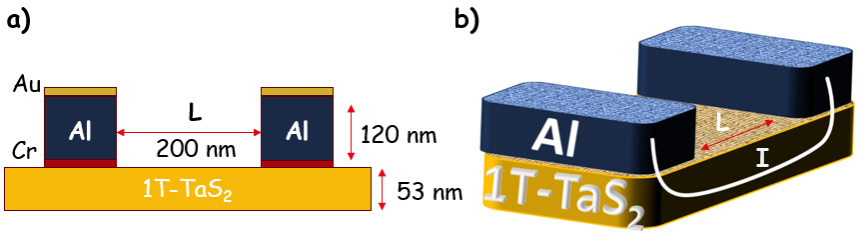

Figure 5.3: **a)** Cross section of a chip having the same structure as the one in fig 5.4. The distance between the electrodes is indicated with L, the Cr (red) is the adhesion layer and Au (yellow) is the capping layer. **b)** 3D structure of a JJ made with the 1T-TaS_2 as inter-layer and Aluminum as superconductor. White line is a qualitative sketch of the path of the supercurrent throughout the junction.

we propose to induce superconductivity in tantalum di-sulfide through the proximity effect, and the developed devices architecture suitable for such purpose is shown in Fig. 5.3.

To achieve this, a milestone assessment of the relevant lengths, materials, as inter-layers and electronics is currently under development. Several attempts, which include different layouts and inter-layers between the coupled materials, former are useful to achieve a better Fermi velocities matching, have been made.

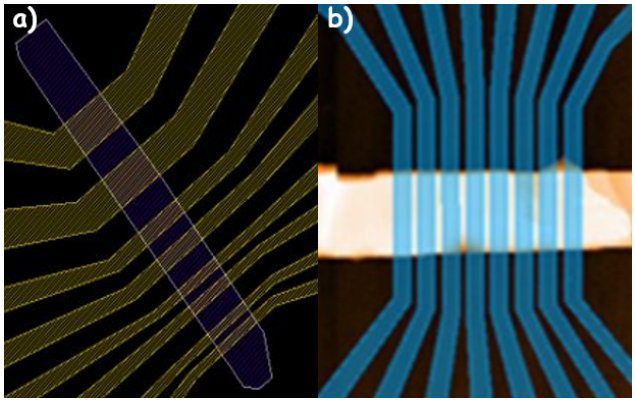

Figure 5.4: **a)** First design of Josephson junctions having different gap lengths, ranging from 1 μm to 200 nm. **b)** Second developed design of an array of Josephson junctions having gaps from 160nm to 200nm.

The fabrication process is developed in collaboration with the Ljubljana University and the characterization was performed at University Federico II of Naples. The junctions show a planar structure and the 1T-TaS_2 layer is clamped by Al 120 nm. A first design developed design included 4 junctions on the same flake with different gaps size ranging from 200 nm to 1 μm (see Fig. 5.4 **a)**. It allows to investigate the transport properties of the devices in both two and four-probe configuration (see appendix C), thus giving a direct measurement of the two-probe resistance R_{2w}, four-probe resistance R_{4w} and the contact resistance R_c of the device under investigation. For example, for the 1T-TaS_2 junctions employing as inter-layer Chromium $R_{2w} = 10.50 \pm 0.02\ k\Omega$ and $R_{4w} = 41 \pm 1\ \Omega$, leading to eastimate $R_c = 5.70 \pm 0.02\ k\Omega$.

Few attempts of making junctions based on 1T-TaS_2 flakes have been made and it differs on the used inter-layer. Fig. 5.5 show the Current-Voltage curves (IVs) for junctions based on Al/TaS_2 having **a)** Cr and an 1T-TaS_2 barrier 330 nm long and **b)** Pd as inter-layer, both having a resistance of the order of tens of $kOhm$.

The Fig. 5.5 **a)** behaves like a typical of semiconductor. A second developed batch of Al/1T-TaS_2 having Titanium (Ti) as inter-layer, where both Al and Ti have been deposited by sputter. Their scanning electron microscope (SEM) and atomic force microscope (AFM) images are shown in Fig. 5.6 **a)** and **b)**. This layout includes smallest gaps ($\approx$ 100 nm), achievable by the used electron beam lithography (EBL) systems. Former sizes are of the same order of normal coherent length ξ_N (section 1.1.6) . However, the analysis made using SEM and AFM show unwanted shorts between Al fingers and the covered 1T-TaS_2 that compromise the electrical characterization of the junctions.

For this reason, a new design (Fig. 5.7) that reduces the e-beam proximity effect has

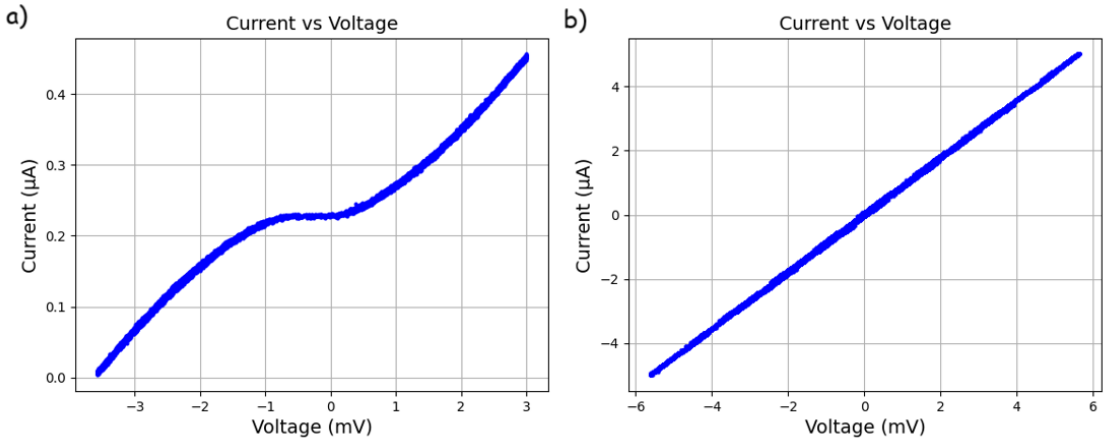

Figure 5.5: **a)** Current - Voltage at 10 *mK* for a Al - 1T-TaS_2 JJs with Cr (3 *nm*) as adhesion layer. **b)** Current - Voltage at 10 *mK* for a Al-TaS2 JJs employing Pd (3 *nm*) as inter-layer.

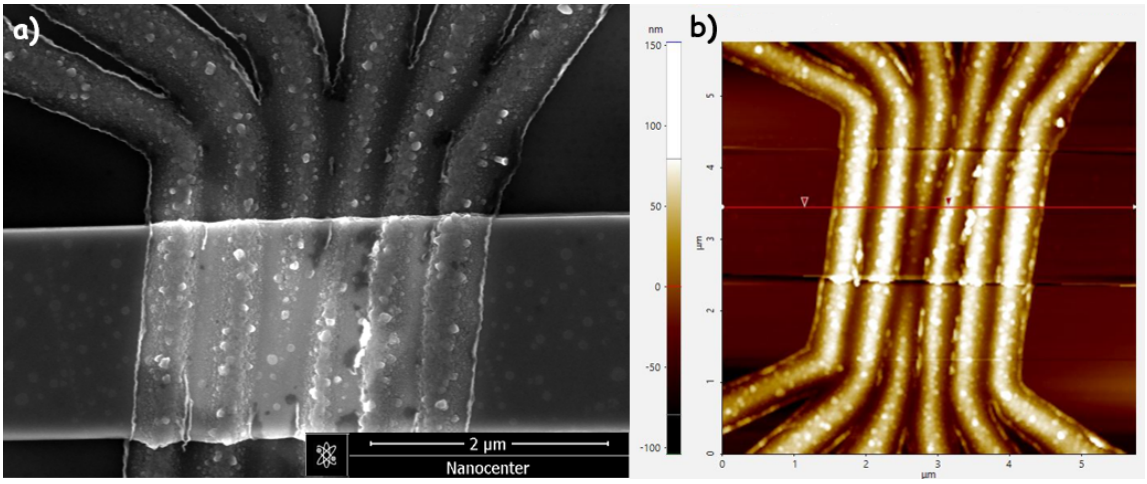

Figure 5.6: **a)**Scanning electron microscope (SEM) image of a set of shorted junctions where the Al has been deposited by sputter. **b)** Atomic force microscope (AFM) image of the same array of JJs. It shows unwanted shorted between the closest fingers.

been considered. To address this issue, a calibration of the fabrication process has been needed; e-beam doses test has been carried out. Fig. 5.7 reports the SEM image of the last

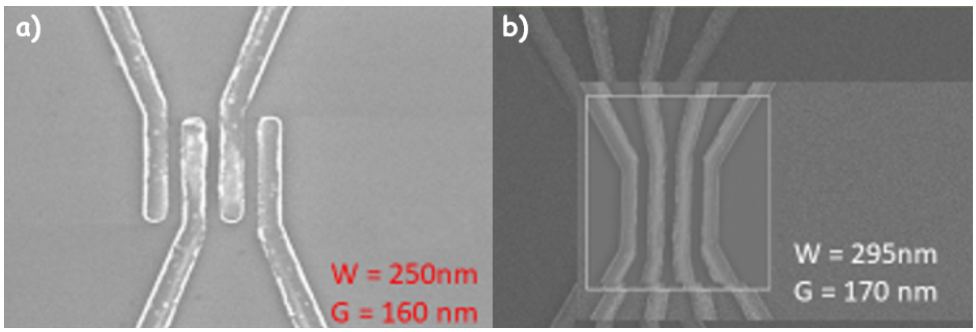

Figure 5.7: **a)** Scanning electron microscope image of an array of Al fingers W = 250 *nm* and of three gaps G = 160 *nm* long. **b)** SEM image of an junction layout with four Aluminum fingers 295 *nm* wide and three gaps of 170 *nm* wide

two layouts under development, where the gap between the fingers is fixed to **a)** 160 *nm* while in Fig. 5.7 **b)** 170 *nm*. These junctions are currently under fabrication and will be soon characterized as a function of the temperature till at the lowest available (10 mK) and by applying electrical pulses ranging from 100 *ns* to 1 μs with an amplitude of the order of 100 mV to $1V$.

5.3 Voltage Pulse Application

As it has been shown in Fig. (5.2) the properties of the 1T-TaS_2 can be tuned by applying a voltage pulse whose amplitude depends on the process (write or erase), on the sample size and on the device characteristics [37] . The pulse width is related to its energy, and ranges from 100 *ms* down to 16 *ps* [58]. Because of that I have made a script that allows to drive a pulse generator and record the data.

The pulse voltage should be applied with a proper amplitude to the device. Because of that, having set the source impedance, the load impedance has to be measured and consequently the pulse amplitude has to be modified in accordance to the drops of voltages [65]. In our case, the voltage pre-amplifier used in the electronic configuration has an

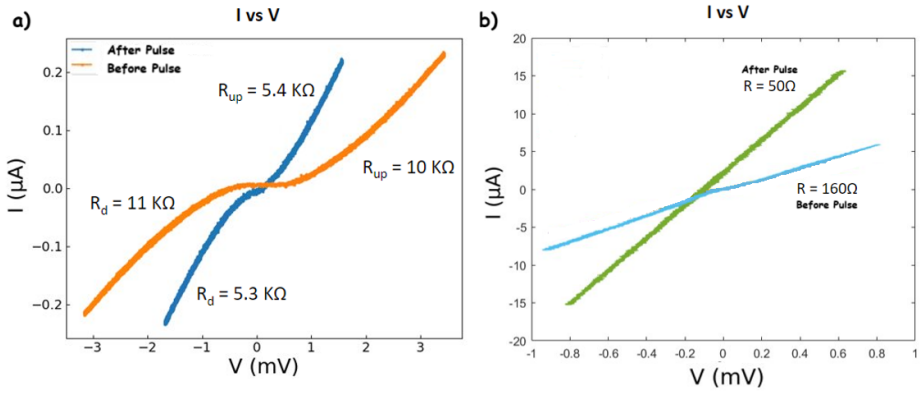

Figure 5.8: **a)** Current - Voltage at 35 *mK* for a Al - 1T-TaS_2 JJs with Cr (3 *nm*) as adhesion layer, showing the pulse effect. **b)** Current - Voltage at 35 *mK* for a Al-TaS2 JJs employing Pd (3 *nm*) as inter-layer, showing the pulse effect.

input voltage impedance of 100 $M\Omega$ [66], allowing to read the pulse on the voltage lines. Knowing the current sent and the resistance of the device, it is possible to estimate the voltage drop across the junction.

Voltage pulses in the range 100 *mV* - 1 *V* having a period of 100 μs were sent on the junctions having chromium and palladium as inter-layers. Results are shown in Fig. 5.8, where **a)** and **b)** show how the application of the pulse changed the junctions properties. A deeper investigation of the physical meaning of this change is currently investigation but elsewhere it has been ascribed to the 1T-TaS_2 flakes properties [37].

Conclusions

In this thesis, we have conducted a comprehensive investigation of Josephson junctions (JJs) in SIS and SIs'FS architectures, where 'S' stands for a superconducting layer of Al or Nb, "s" denotes a thin layer of superconductor, "I" refers to an insulating barrier and "F" represents a thin ferromagnetic material, specifically Permalloy. The ferromagnetic JJs were meticulously fabricated through a combination of deposition, etching and optical lithography steps optimized in collaboration with the "Istituto di Scienze Applicate e Sistemi Intelligenti" E. Caianiello "ISASI-CNR-Pozzuoli (Italy)". Magneto transport measurements have been carried out down to 10 mK and I have also made scripts, by using both Matlab and Python, for the data analysis, recording and remote interface programming.

Current-voltage measurements have been compared with the theoretical models, providing valuable insights in both SIS and SIs'FS architectures employing Al and Nb. In particular, we have fabricated and characterized junctions having Al as superconducting banks and a thin ferromagnetic layer (Py) as a barrier.

The ferromagnetic junctions based on Al material also make it feasible to access a regime in which the Josephson energy $E_j \approx I_c$ is bigger than energy $Ec \approx 1/C$, but remains measurable using our experimental RF setup (4-8 GHz). These results set the stage for the exploration of the fundamental properties of SIS and SIs'FS JJs, which could be leveraged in novel architectures for qubits, achieved by coupling superconducting resonant circuits with ferromagnetic junctions. The inclusion of the ferromagnetic layer 'F' in these junctions adds an extra degree of freedom, opening up to the development of a next generation of Trasmon qubit devices, also referred to as "Ferro-Trasmon".

Hybrid junctions using a Van der Waals material were also analyzed in their embryonic phase. The investigated architecture represents the starting point towards more advanced junction's layout based on Van der Waals ferromagnetic materials that if are coupled to the superconductors could give rise to the pair correlations and an induced superconductivity over much longer distances (hundreds nanometers against the few tens nanometer in the conventional ferromagnetic Josephson junctions).

In this project I contributed to the design, measure as a function of the temperature and the application of electrical nano-pulses to the built junctions. I have also developed all the Matlab codes useful to drive the electrical setup, record and analyze the experimental data. The endeavor of working with hybrid junctions has been executed with precision at the nanoscale level, with the primary objective of enhancing chip layouts to mitigate manufacturing challenges. Efforts have been put towards the creation of nano gaps,

between the Al contacts and to achieve high transparent interfaces between the coupled materials, all in pursuit of making high quality Josephson Junctions. The characterization of the first batches of hybrid junctions was carried out, which has provided excellent insights into manufacturing issues, thus allowing to improve the next generation of Josephson Junction based on 1T-TaS_2 Van der Waals material.

Appendix A
Josephson Equations Derivation

We will discuss only the most basic aspects of this topic, which are noteworthy due to both their fundamental implications and technological applications. Consider a scenario with two superconductors, whether they are made of the same or different materials, separated by a thin insulating barrier of width "b," as illustrated in Fig. In the situation where the insulating barrier is infinitely thick, the superconductor on the left side can be described by an order parameter "ψ_1". This parameter can be expressed as:

$$\psi_1 = |\psi_1| \cdot e^{i\theta_1} \tag{A.1}$$

Here, both $|\psi_1|$ and θ_1 remain constant throughout the entire volume of superconductor 1. Similarly, the superconductor on the right side is characterized by another order parameter "ψ_2," given by:

$$\psi_2 = |\psi_2| \cdot e^{i\theta_2} \tag{A.2}$$

In this case, $|\psi_2|$ and θ_2 are independent of spatial location within superconductor 2's volume. When these two superconductors are separated by a thin insulating barrier, we can anticipate that the superconducting order parameters ψ_1 and ψ_2 will decay within the insulating region. It's reasonable to assume that the order parameter $\psi(z)$ within the barrier can be represented as follows:

$$\psi(z) = \psi_1 \cdot e^{-\beta z} + \psi_2 \cdot e^{\beta(z-b)}, \quad 0 < z < b \tag{A.3}$$

Inserting Eq. A.3 into the Ginzburg-Landau equation 1.11 while considering negligible magnetic fields yields:

$$\begin{aligned} J_s(z) &= -\frac{i\hbar e^*}{2m^*}\left(\psi^*(z)\frac{d\psi(z)}{dz} - \psi(z)\frac{d\psi^*(z)}{dz}\right) \\ &= -\frac{i\hbar e^*}{m}\beta e^{-\beta b}(\psi_1^*\psi_2 - \psi_1\psi_2^*) \\ &= \frac{2\hbar e^*}{m^*}\beta e^{-\beta b}|\psi_1| \cdot |\psi_2| \cdot \sin(\theta_2 - \theta_1) \end{aligned}$$

$J_s(z)$ represents the current density at position "z". It is determined by the product of various physical constants and characteristics of the superconductors. In the presence

of an insulating barrier, the current density is influenced by the phase difference ($\theta_2 - \theta_1$) between the order parameters of the two superconductors. This phase difference contributes to the sinusoidal behavior of the current density within the barrier. The factor "β" characterizes the damping effect within the barrier, influencing the extent to which the order parameters decay. The physical interpretation of this equation lies in its depiction of how superconducting properties, order parameter phase differences, and barrier characteristics combine to influence the flow of current between superconductors.

We thus observe that the Josephson supercurrent, which flows between two superconductors separated by an insulating barrier, is linked to the phase difference $\phi = \theta_2 - \theta_1$ of the order parameters in the two superconductors by the equation:

$$I = I_c \sin \phi \tag{A.4}$$

Here, I_c depends on the geometric and physical characteristics of the junction.

Consider now a superconducting junction biased with a voltage V, which could be either constant or time-dependent. When a potential difference is established between the two superconductors, the relative energy difference between Cooper pairs belonging to these superconductors becomes $2eV$. Similar to the quantum mechanical rate of phase change for ordinary eigenfunctions (where energy is divided by $\hbar$), we can expect the time variation of the relative phase ϕ to be:

$$\frac{d\phi}{dt} = \frac{2eV}{\hbar} \tag{A.5}$$

If the potential V across the SIS (superconductor-insulator-superconductor) junction is zero, ϕ remains constant. From Eq A.4, we deduce that a supercurrent with an intensity ranging from $-I_c$ to $+I_c$ can flow through the junction (the exact value is determined by the external circuit). This phenomenon is responsible for the appearance of a zero-resistance spike at $V = 0$ in the current-voltage ($I - V$) characteristics of a Josephson junction.

Appendix B
Data Analysis Scripts

During my thesis I had the opportunity to work with two programming languages: Matlab and Python. Thanks to these I wrote several scripts, with which I carried out a careful and accurate data analysis, trying to make these scripts easy to use not only for myself but also for the other members of my team. These scripts can be found at the following link : https://github.com/Marguar/MasterThesis.git.

Below is a brief description of the most important ones :

- **IV Trace Acq.mlx** : Matlab Live Script used for analyzing data just taken from the oscilloscope. In addition to carrying out a conversion, taking into account the various amplification factors, saving the data in .dat format, it proceeded with a rapid analysis of the data with respective plots, giving a rapid and quick estimate of some important quantities such as critical current and normal resistance.

- **IV An** : This Matlab Live Script performs a more accurate analysis, taking the .dat files saved with the other script. Specifically, it takes into account the different temperatures at which the current-voltage curves were recorded and carries out a targeted analysis, taking into account a very precise number of these.

- **Tana.ipynb** : This is a Jupyter Notebook, complementary to the IV An, which performs a temperature analysis with different criteria to evaluate the critical current and also estimates the normal resistance as well as various plots.

- **MagneticField.ipynb** : This is a Jupyter Notebook used for analyzing current voltage curves in magnetic field. This takes as input two folders containing the .dat files relating to the current-voltage curves, taken via the LabView program, makes an estimate of the critical current for each of these, carrying out a series of explanatory plots.

- **Cond.ipynb** : This is a Jupyter Notebook which analyzes the conductance curves, divided by short and long ranges, respectively for voltage values less and greater than the superconducting gap, giving an approximate estimate of the latter.

At the end of the Matlab scripts there are several local functions used as a library, while the file **Fun.py** is the library used for the Python scripts.

Appendix C
4 Probe Measure

Four-probe measurement, also known as a four-point probe measurement, is a technique used in electrical and materials characterization to accurately measure the electrical resistivity or conductivity of a material. It involves the use of four evenly spaced electrical contacts (probes) on a material surface. Two of the probes are used to apply a known current (current probes), while the other two probes measure the resulting voltage (voltage probes). This arrangement minimizes errors introduced by the resistance of the connecting wires and contacts. This method is particularly useful when dealing with thin films, semiconductors, and materials with low resistivity values. In contrast, two-probe measurements involve only two contacts, one for applying current and the other for measuring voltage. While two-probe measurements are simpler and faster, they are less accurate, especially for materials with low resistivity. The contact resistance can significantly affect the measured resistance, leading to erroneous results. By carrying out both a 2-contact and a 4-contact measurement it is possible to estimate the contact resistance :

$$R_{2w} = R_{4w} + 2R_c \quad \longrightarrow \quad R_c = \frac{R_{2w} - R_{4w}}{2} \tag{C.1}$$

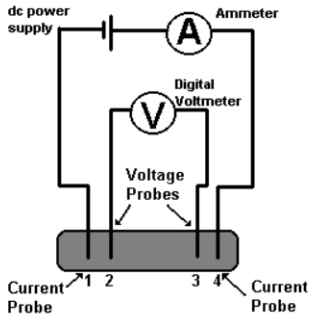

Figure C.1: An example of a four-probe measurement, the current passes through 2 lines while the other two are used only to estimate the voltage.

Appendix D
Instruments

Agilent 33120 Arbitrary WaveFunction Generator

The Agilent 33120 is a reliable and versatile function/arbitrary waveform generator manufactured by Agilent Technologies (now known as Keysight Technologies) [67]. Its broad frequency range, precise waveform control, modulation capabilities, and connectivity options make it a valuable tool for engineers, scientists, and students working with analog and digital circuits. It is commonly used in electronics laboratories, research facilities, and educational institutions.
Key Features:

- **Waveform Generation**: The Agilent 33120 can generate various types of waveforms, including sine, square, triangle, ramp, and pulse signals. It supports both standard waveforms and arbitrary waveforms, allowing users to define their own custom waveforms with precise control over frequency, amplitude, and other parameters.

- **Frequency Range**: It offers a wide frequency range from $100\mu Hz$ to $15MHz$, enabling the generation of signals across a broad spectrum. The generator also provides fine frequency resolution, allowing users to set precise frequencies.

Figure D.1: Agilent 33120 Arbitrary WaveFunction Generator [67].

Figure D.2: Keithley 2400 Source Meter [68].

- **Amplitude Control**: The instrument allows for accurate control of signal amplitude, offering adjustable output voltages from $10mV$ to $10V$ peak-to-peak. It provides high signal integrity and low distortion levels, ensuring reliable and accurate waveform generation.

- **Multiple Connectivity Options**: The instrument offers multiple connectivity options, including USB and GPIB (General Purpose Interface Bus), allowing seamless integration with computer systems and other test equipment. This enables remote control, data logging, and automation of waveform generation tasks.

Keithley 2400 Source Meter

The Keithley 2400 is a highly capable and accurate source meter unit designed for a wide range of electrical measurement and sourcing applications [68]. Its precise control, measurement capabilities, compliance ranges, and software interfaces make it a valuable tool for researchers, engineers, and scientists working with semiconductor devices, materials, and other electronic components.
Key Features:

- **Voltage and Current Sourcing**: The Keithley 2400 can function as both a voltage source and a current source. It provides precise control over the sourced voltage and current levels, allowing users to generate specific electrical signals for testing and characterization purposes.

- **Measurement Capabilities**: In addition to sourcing, the 2400 offers highly accurate measurements of voltage, current, and resistance. It can measure voltage and current levels with high resolution and low noise, enabling precise characterization of devices under test (DUTs).

- **Source and Measurement Modes**: The instrument supports both two-wire and four-wire measurement configurations, providing flexibility for different types of measurements. In the two-wire mode, it combines the sourcing and measurement functions using the same two wires, while the four-wire mode separates the sourcing and measurement paths for accurate resistance measurements.

Figure D.3: Keithley 3402 Pulse Pattern Generator [65].

- **Built-in Software Interfaces**: The instrument features built-in software interfaces such as GPIB (General Purpose Interface Bus), USB, and LAN (Local Area Network). These interfaces enable seamless integration with computer systems, remote control, and data transfer for efficient test automation and data analysis.

Keithley 3402 Pulse Pattern Generator

The Keithley 3401/3402 pulse pattern generators are versatile instruments designed for generating precise and customize pulse patterns for testing and characterization applications [65]. Their features such as pulse generation, high timing resolution, variable amplitude, flexible triggering, memory and sequencing, user-friendly interface, and connectivity options make them valuable tools for researchers, engineers, and scientists working with digital systems, semiconductor devices, and other applications requiring accurate pulse generation and pattern control.
Key Features:

- **Pulse Generation**: The Keithley 3401/3402 pulse pattern generators can generate a wide range of pulse patterns with precise control over parameters such as pulse width, pulse delay, repetition rate, and amplitude. They allow users to define complex pulse sequences and patterns to simulate real-world scenarios.
- **High Timing Resolution**: These pulse pattern generators offer high timing resolution, allowing for precise control and synchronization of pulse edges. This enables accurate timing measurements and characterization of devices under test (DUTs) with fast response times.
- **Variable Amplitude**: The instruments provide adjustable pulse amplitudes to match the requirements of the DUTs. The amplitude can often be controlled in both positive and negative polarities, allowing for versatile testing in various signal environments.
- **Flexible Triggering**: The Keithley 3401/3402 pulse pattern generators offer flexible triggering options to initiate the pulse patterns. They typically support internal triggering, external triggering via external sources or signals, and software triggering for precise synchronization with other test equipment.

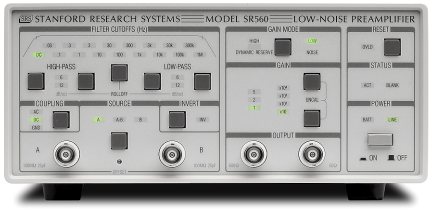

Figure D.4: SR560 Low-Noise Voltage Preamplifier [66].

- **Multiple Outputs**: These pulse pattern generators typically offer multiple output channels, allowing for simultaneous generation of different pulse patterns or synchronization with other instruments for complex testing setups.
- **Connectivity and Software Support**: The Keithley 3401/3402 pulse pattern generators typically offer connectivity options such as USB, Ethernet, and GPIB for remote control and data transfer.

SR560 Low-Noise Voltage Preamplifier

The SR560 is a versatile and high-performance low-noise preamplifier designed for amplifying weak signals with minimal noise interference manufactured by Stanford Research Systems (SRS) [66]. Its low noise characteristics, wide bandwidth, adjustable gain, and selectable filters make it an essential tool for precision measurements, signal conditioning, and scientific research in various fields, including physics, chemistry, electronics, and materials science.
Key features:

- **Low Noise Amplification**: The SR560 offers exceptional low-noise performance, allowing it to amplify weak signals while maintaining high fidelity. It has a very low input noise density, typically in the range of a few $nV/\sqrt{Hz}$, making it suitable for amplifying small signals in sensitive measurement applications.
- **Wide Bandwidth**: The pre-amplifier provides a wide bandwidth, typically ranging from DC (Direct Current) to 100 kHz. This broad frequency response enables it to capture signals across a wide spectrum, making it suitable for a variety of scientific and industrial applications.
- **Adjustable Gain**: The SR560 offers adjustable gain settings, allowing users to select the appropriate amplification factor for their specific needs. It provides a wide dynamic range[1], accommodating signals ranging from microvolts to volts with high precision.

[1]Dynamic range is the ratio between the largest and smallest values that a certain quantity can assume. It is measured either as a ratio or as a base-10 (decibel) or base-2 (doublings, bits or stops) logarithmic value of the difference between the smallest and largest signal values

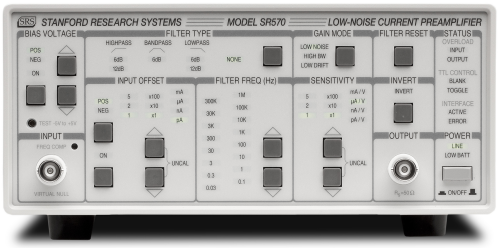

Figure D.5: SR570 Low-Noise Current Preamplifier [69].

- **Filter Options**: The pre-amplifier features selectable input filters to further enhance signal conditioning. These filters include low-pass, high-pass, and notch filters, which can be employed to suppress noise, eliminate unwanted frequencies, and improve signal quality in specific frequency bands.

SR570 Low-Noise Current Pre-amplifier

The SR570 is a versatile and high-performance low-noise current preamplifier manufactured by Stanford Research Systems (SRS) it is designed for precise current amplification and measurement [69]. The SR570 is designed to amplify low-level current signals while maintaining low noise levels, making it suitable for sensitive current measurements in various scientific and research applications.
Key Features:

- **Low Noise Amplification**: The SR570 offers exceptional low-noise performance, enabling the amplification of weak current signals with high fidelity. It features a low input noise density, typically in the range of a few $fA/\sqrt{Hz}$, making it suitable for amplifying small currents in sensitive measurement applications.

- **Wide Bandwidth**: The preamplifier provides a wide bandwidth, typically ranging from DC (Direct Current) to $1MHz$. This broad frequency response allows it to capture current signals across a wide spectrum, making it useful in a variety of scientific and industrial applications.

- **Adjustable Gain**: The SR570 allows for adjustable gain settings, enabling users to select the appropriate amplification factor based on the specific measurement requirements. It provides a wide dynamic range, accommodating currents ranging from picoamps to milliamps with high precision.

SR830 Lock-In Amplifier

The SR830 is a powerful and versatile lock-in amplifier designed for precision measurement and analysis of low-level AC signals [70]. Its lock-in amplification techniques, dual-phase detection, wide frequency range, low-noise performance, and advanced analysis

Figure D.6: SR830 Lock-In Amplifier[70].

capabilities make it a valuable tool for researchers, scientists, and engineers working on applications requiring sensitive signal detection, noise rejection, and frequency domain analysis.
Key Features:

- **Lock-In Amplification**: The SR830 utilizes lock-in amplification techniques to extract and measure small AC signals buried in noise or other interference. It employs a reference signal, typically generated by an external oscillator, to demodulate the measured signal and extract its amplitude and phase information accurately.
- **Dual-Phase Detection**: The SR830 offers dual-phase detection capabilities, allowing simultaneous measurement of both in-phase and quadrature components of the input signal. This enables precise determination of amplitude, phase, and other signal parameters, making it suitable for a wide range of applications requiring accurate signal analysis.
- **Frequency Range and Resolution**: The lock-in amplifier provides a wide frequency range, typically spanning from $1mHz$ to $102.4kHz$. It offers excellent frequency resolution, allowing users to finely tune the measurement frequency and analyze signals with high precision.
- **Low-Noise Performance**: The SR830 is designed to achieve extremely low noise levels, ensuring high signal fidelity and sensitivity. It features a low-noise front-end amplifier and advanced signal processing techniques to minimize noise contributions and improve the signal-to-noise ratio.
- **Remote Control and Data Transfer**: The SR830 supports remote control via various interfaces, including GPIB (General Purpose Interface Bus), USB, and RS-232. This enables seamless integration into automated measurement systems and facilitates remote programming, data acquisition, and analysis.

Figure D.7: HDO 6000 Oscilloscope [71].

HDO 6000 Oscilloscope

The HDO6000 Oscilloscope is a high-definition oscilloscope that combines Teledyne LeCroy's HD4096 high-definition technology with long memory, a compact form factor, 12.1" touch screen display, powerful measurement and analysis tools, and mixed signal capability [71]. In particular the HD4096 high definition technology consists of high sample rate 12-bit ADCs, high signal-to-noise ratio amplifiers and a low-noise system architecture. This technology enables high definition oscilloscopes to capture and display signals of up to 1 GHz with high sample rate and 16 times more resolution than other oscilloscopes. It is ideal for circuit validation, system debug and waveform analysis. The HDO6000 Oscilloscope has up to 250 Mpts of memory which can capture large amounts of data oscilloscopes. The 2.5 GS/s, 250 Mpts architecture provides the ability to capture a fast transient or a long acquisition. Moreover, The HDO6000 Oscilloscope has also a spectrum analyzer mode that provides a spectrum analyzer style user interface simplifying how frequency content is viewed and analyzed.

Bibliography

[1] G. Hu, C. Wang, S. Wang, and altri. "Long-range skin Josephson supercurrent across a van der Waals ferromagnet". In: *Nature Communications* 14 (2023), p. 1779. DOI: 10.1038/s41467-023-37603-9.

[2] Antonio Vettoliere et al. "High-Quality Ferromagnetic Josephson Junctions Based on Aluminum Electrodes". In: *Nanomaterials* 12.23 (2022). ISSN: 2079-4991. DOI: 10.3390/nano12234155. URL: https://www.mdpi.com/2079-4991/12/23/4155.

[3] Roberta Satariano. "PhD thesis: Magnetic tunnel Josephson Junctions towards hybrid quantum architectures". PhD thesis. University of Naples Federico II, 2023.

[4] K. Rossnagel. "On the origin of charge-density waves in select layered transition-metal dichalcogenides". In: *Journal of Physics Condensed Matter* 23.21, 213001 (June 2011), p. 213001. DOI: 10.1088/0953-8984/23/21/213001.

[5] H.K. Onnes. "The resistance of pure mercury at helium temperatures". In: *Comm. Leiden* (Apr. 1911).

[6] W. Meissner and R. Ochsenfeld. "Ein neuer Effekt bei Eintritt der Supraleitfähigkeit". German. In: *Die Naturwissenschaften* 21.44, 787 (1933), pp. 787–788. ISSN: 0028-1042. DOI: 10.1007/bf01504252.

[7] F. London and H. London. "The electromagnetic equations of the supraconductor". In: *Proc. Roy. Soc. (London)* A149 (1935), p. 71. ISSN: 0080-4630.

[8] L.P. Gorkov. "Microscopic derivation of the Ginzburg-Landau equations in the theory of superconductivity". In: *Soviet Physics JETP* 36.6 (1959). URL: http://www.jetp.ac.ru/cgi-bin/dn/e_009_06_1364.pdf.

[9] A.A. Abrikosov. "On the magnetic properties of superconductors of the second group". In: *Soviet Physics JETP* 5 (1957), p. 1174.

[10] Emanuel Maxwell. "Isotope Effect in the Superconductivity of Mercury". In: *Physical Review* 78.4, 477 (May 1950), p. 477. ISSN: 0031-899X. DOI: 10.1103/physrev.78.477.

[11] C. A. Reynolds, B. Serin, W. H. Wright, and L. B. Nesbitt. "Superconductivity of Isotopes of Mercury". In: *Physical Review* 78.4, 487 (1950), p. 487. ISSN: 0031-899X. DOI: 10.1103/physrev.78.487.

[12] J. Bardeen, L. N. Cooper, and J. R. Schrieffer. “Theory of Superconductivity”. In: *Physical Review* 108.5, 1175 (Dec. 1957), pp. 1175–1204. ISSN: 0031-899X. DOI: 10.1103/physrev.108.1175. URL: https://doi.org/10.1103/physrev.108.1175.

[13] Giuseppe Grosso and Giuseppe Pastori Parravicini. *Solid State Physics*. Academic Press, 2014. ISBN: 9780123850317.

[14] B.D. Josephson. “Possible new effects in superconductive tunnelling”. In: *Physics Letters* 1.7 (1962), pp. 251–253. ISSN: 0031-9163. DOI: http://dx.doi.org/10.1016/0031-9163(62)91369-0. URL: http://www.sciencedirect.com/science/article/pii/0031916362913690.

[15] J. G. Bednorz and K. A. Müller. “Possible high Tc superconductivity in the Ba-La-Cu-O system”. In: *Z. Phys. B* 64.2 (1986), p. 189.

[16] M. Tinkham. *Introduction to Superconductivity*. 2nd. McGraw Hill, Inc., 1996.

[17] Charles Kittel. *Introduction to Solid State Physics*. 1st. John Wiley and Sons, 1953, p. 396. ISBN: 978-1-119-45416-8.

[18] A. Vettoliere et al. “Aluminum-ferromagnetic Josephson tunnel junctions for high quality magnetic switching devices”. In: *Applied Physics Letters* 120.26 (June 2022), p. 262601. ISSN: 0003-6951. DOI: 10.1063/5.0101686. eprint: https://pubs.aip.org/aip/apl/article-pdf/doi/10.1063/5.0101686/16450324/262601_1_online.pdf. URL: https://doi.org/10.1063/5.0101686.

[19] Tero T. Heikkilä. *The Physics of Nanoelectronics*. First. © Tero T. Heikkilä 2013. Oxford University Press, 2013.

[20] P.G. de Gennes. *Superconductivity of Metals and Alloys*. Westview Press, 1999.

[21] Vinay Ambegaokar and Alexis Baratoff. “Tunneling Between Superconductors”. In: *Phys. Rev. Lett.* 10 (11 June 1963), pp. 486–489. DOI: 10.1103/PhysRevLett.10.486. URL: https://link.aps.org/doi/10.1103/PhysRevLett.10.486.

[22] K. K. Likharev. “Superconducting weak links”. In: *Rev. Mod. Phys.* 51 (1 Jan. 1979), pp. 101–159. DOI: 10.1103/RevModPhys.51.101. URL: https://link.aps.org/doi/10.1103/RevModPhys.51.101.

[23] Francesco Tafuri. *Fundamentals and Frontiers of the Josephson Effect*. Springer Series in Materials Science. Springer, 2019. ISBN: 978-3-030-20724-3. DOI: 10.1007/978-3-030-20726-7.

[24] A.F. Andreev. “A.F. Andreev”. In: *Soviet Physics JETP* 19 (1964), p. 1228.

[25] A. Barone and G. Paternò. *Physics and Application of the Josephson Effect*. John Wiley & Sons, 1982.

[26] S. Datta. *Electronic Transport in Mesoscopic Systems*. Cambridge University Press, 1995.

[27] Konstantin K. Likharev. *Dynamics of Josephson Junctions and Circuits*. 1st Edition. London: Routledge, 1986, p. 640. ISBN: 9781315141572.

[28] Chuan Li, S. Guéron, A. Chepelianskii, and H. Bouchiat. "Full range of proximity effect probed with superconductor/graphene/superconductor junctions". In: *Phys. Rev. B* 94 (11 Sept. 2016), p. 115405. DOI: 10.1103/PhysRevB.94.115405. URL: https://link.aps.org/doi/10.1103/PhysRevB.94.115405.

[29] M. G. Flokstra. "Proximity effects in superconducting spin-valve structures". PhD thesis. Casimir PhD Series, Feb. 2010. URL: https://hdl.handle.net/1887/14751.

[30] A. I. Buzdin. "Proximity effects in superconductor-ferromagnet heterostructures". In: *Rev. Mod. Phys.* 77 (2005), pp. 935–976. URL: http://link.aps.org/doi/10.1103/RevModPhys.77.935.

[31] A. Larkin and Y. Ovchinnikov. "Inhomogeneous state of superconductors". In: *Soviet Physics JETP* 20 (1964), p. 762.

[32] Halima Giovanna Ahmad. "Master thesis: Physics of the Josephson effect in junctions with ferromagnetic barriers". MA thesis. University of Naples ' Federico II, 2017.

[33] Halima Giovanna Ahmad. "PhD thesis: Physics of the Josephson effect in junctions with ferromagnetic barriers towards quantum circuits and RF applications". PhD thesis. University of Naples Federico II, 2021.

[34] Gregory L. Baker and James A. Blackburn. *The Pendulum: A Case Study in Physics*. 1st. New York: Oxford University Press Inc., 2005.

[35] S. V. Bakurskiy et al. "Theoretical model of superconducting spintronic SIsFS devices". In: *Applied Physics Letters* 102.19 (2013), p. 192603. DOI: 10.1063/1.4805032. URL: https://doi.org/10.1063/1.4805032.

[36] Oxford Instruments Nanoscience. *Tryton Cryofree Dilution Refrigerator: Principles of Operation*. Version 4.0.1. Manual. Oxford Instruments Nanoscience. Tubney Woods, Abingdon, United Kingdom, 2016.

[37] Anze Mraz et al. "Charge Configuration Memory Devices: Energy Efficiency and Switching Speed". In: *Nano Letters* 22.12 (2022). PMID: 35688423, pp. 4814–4821. DOI: 10.1021/acs.nanolett.2c01116. eprint: https://doi.org/10.1021/acs.nanolett.2c01116. URL: https://doi.org/10.1021/acs.nanolett.2c01116.

[38] Kulicke and Soffa Industries, Inc. *Kulicke and Soffa Model 4526 Wire Bonder: User's Manual*. Manual.

[39] Loredana Parlato et al. “Characterization of scalable Josephson memory element containing a strong ferromagnet”. In: *Journal of Applied Physics* 127.19 (May 2020), p. 193901. ISSN: 0021-8979. DOI: 10.1063/5.0004554. eprint: https://pubs.aip.org/aip/jap/article-pdf/doi/10.1063/5.0004554/15244693/193901_1_online.pdf. URL: https://doi.org/10.1063/5.0004554.

[40] D. Massarotti et al. “Electrodynamics of Josephson junctions containing strong ferromagnets”. In: *Phys. Rev. B* 98 (14 Oct. 2018), p. 144516. DOI: 10.1103/PhysRevB.98.144516. URL: https://link.aps.org/doi/10.1103/PhysRevB.98.144516.

[41] V.V. Bol’ginov, V.S. Stolyarov, D.S. Sobanin, and et al. “Magnetic switches based on Nb-PdFe-Nb Josephson junctions with a magnetically soft ferromagnetic interlayer”. In: *Journal of Experimental and Theoretical Physics Letters (Jetp Lett)* 95 (2012), pp. 366–371. DOI: 10.1134/S0021364012070028.

[42] Roberta Satariano et al. “Inverse magnetic hysteresis of the Josephson supercurrent: Study of the magnetic properties of thin niobium/permalloy interfaces”. In: *Physical Review B* 103.22 (June 2021), p. 224521. DOI: 10.1103/physrevb.103.224521. URL: https://doi.org/10.1103/physrevb.103.224521.

[43] I. A. Golovchanskiy et al. “Magnetization dynamics in dilute $Pd_{1-x}Fe_x$ thin films and patterned microstructures considered for superconducting electronics”. In: *Journal of Applied Physics* 120.16 (2016), p. 163902. DOI: 10.1063/1.4965991. URL: https://doi.org/10.1063/1.4965991.

[44] Roberta Caruso et al. “Ferromagnetic Josephson Junctions for High Performance Computation”. In: *Proceedings* 12.1 (2019). ISSN: 2504-3900. DOI: 10.3390/proceedings2019012016. URL: https://www.mdpi.com/2504-3900/12/1/16.

[45] Halima Giovanna Ahmad et al. “Hybrid ferromagnetic transmon qubit: Circuit design, feasibility, and detection protocols for magnetic fluctuations”. In: *Physical Review B* 105.21 (June 2022), p. 214522. DOI: 10.1103/physrevb.105.214522. URL: https://doi.org/10.1103/physrevb.105.214522.

[46] Roberta Caruso et al. “Properties of Ferromagnetic Josephson Junctions for Memory Applications”. In: *IEEE Transactions on Applied Superconductivity* 28.7 (Oct. 2018), pp. 1–6. DOI: 10.1109/tasc.2018.2836979. URL: https://doi.org/10.1109%2Ftasc.2018.2836979.

[47] Halima Giovanna Ahmad, Luca Di Palma, Roberta Caruso, and et al. “Critical Current Suppression in Spin-Filter Josephson Junctions”. In: *Journal of Superconductivity and Novel Magnetism* 33 (2020), pp. 3043–3049. DOI: 10.1007/s10948-020-05577-0.

[48] R. Caruso et al. “RF assisted switching in magnetic Josephson junctions”. In: *Journal of Applied Physics* 123.13 (2018), p. 133901. DOI: 10.1063/1.5018854. URL: https://doi.org/10.1063/1.5018854.

[49] Kazuko Motizuki, ed. *Structural Phase Transitions in Layered Transition Metal Compounds*. 1st ed. Physics and Chemistry of Materials with A. Springer Dordrecht, 1986, pp. IX, 300. DOI: 10.1007/978-94-009-4576-0.

[50] P. Fazekas and E. Tosatti. "Electrical, structural and magnetic properties of pure and doped 1T-TaS2". In: *Philosophical Magazine B* 39.3 (1979), pp. 229–244. DOI: 10.1080/13642817908245359.

[51] R. E. Thomson, B. Burk, A. Zettl, and J. Clarke. "Scanning tunneling microscopy of the charge-density-wave structure in 1T-TaS2". In: *Physical Review B* 49.24 (June 1994), pp. 16899–16916. DOI: 10.1103/PhysRevB.49.16899. URL: https://doi.org/10.1103/PhysRevB.49.16899.

[52] Rok Venturini et al. "Ultraefficient resistance switching between charge ordered phases in 1T-TaS_2 with a single picosecond electrical pulse". In: *Applied Physics Letters* 120.25, 253510 (June 2022), p. 253510. DOI: 10.1063/5.0096850. arXiv: 2202.13831 [cond-mat.str-el].

[53] F.J. Di Salvo and J.E. Graebner. "The low temperature electrical properties of 1T-TaS2". In: *Solid State Communications* 23.11 (1977), pp. 825–828. ISSN: 0038-1098. DOI: https://doi.org/10.1016/0038-1098(77)90961-9. URL: https://www.sciencedirect.com/science/article/pii/0038109877909619.

[54] Doohee Cho et al. "Nanoscale manipulation of the Mott insulating state coupled to charge order in 1T-TaS2". English. In: *Nature communications* 7 (Jan. 2016). ISSN: 2041-1723. DOI: 10.1038/ncomms10453.

[55] J. Ravnik et al. "A time-domain phase diagram of metastable states in a charge ordered quantum material". In: *Nature Communications* 12.1 (Dec. 2021), p. 2323.

[56] B. Sipos, A. Kusmartseva, A. Akrap, et al. "From Mott state to superconductivity in 1T-TaS2". In: *Nature Materials* 7 (2008), pp. 960–965.

[57] Damjan Svetin, Igor Vaskivskyi, Serguei Brazovskii, and Dragan Mihailovic. *Three-dimensional resistivity switching between correlated electronic states in 1T-TaS2*. 2016. DOI: 10.48550/arXiv.1603.06214. arXiv: 1603.06214 [cond-mat.mes-hall].

[58] Igor Vaskivskyi et al. "Controlling the metal-to-insulator relaxation of the metastable hidden quantum state in 1T-TaS₂". In: *Science Advances* 1.6 (2015), e1500168. DOI: 10.1126/sciadv.1500168. eprint: https://www.science.org/doi/pdf/10.1126/sciadv.1500168. URL: https://www.science.org/doi/abs/10.1126/sciadv.1500168.

[59] A. A. Golubov, M. Yu. Kupriyanov, and E. Il'ichev. "The current-phase relation in Josephson junctions". In: *Rev. Mod. Phys.* 76 (Apr. 2004), pp. 411–469. URL: http://link.aps.org/doi/10.1103/RevModPhys.76.411.

[60] Domenico Montemurro. "Hybrid superconducting InAs-nanowire based nanojunctions". PhD thesis. University of Naples Federico II, 2016.

[61] A. Y. Kitaev. “Fault-tolerant quantum computation by anyons”. In: *Annals of Physics* 303 (Jan. 2003), pp. 2–30.

[62] D. A. Ivanov. “Non-abelian statistics of half-quantum vortices in p-wave superconductors”. In: *Phys Rev Lett* 86 ().

[63] V. Mourik et al. “Signatures of Majorana Fermions in Hybrid Superconductor-Semiconductor Nanowire Devices”. In: *Science* 336 (May 2012), pp. 1003–1007.

[64] A. Das et al. “Zero-bias peaks and splitting in an Al-InAs nanowire topological superconductor as a signature of Majorana fermions”. In: *Nature Physics* 8 (Dec. 2012), pp. 887–895.

[65] Keithley Instruments, Inc. *Series 3400 Pulse Pattern Generators User’s Manual*. Manual. Keithley Instruments, Inc. 28775 Aurora Road, Cleveland, Ohio 44139, Jan. 2007.

[66] Stanford Research Systems. *MODEL SR560 Low-Noise Preamplifier*. Manual. Stanford Research Systems. 1290-D Reamwood Avenue, Sunnyvale, CA 94089 U.S.A., Aug. 2013.

[67] Agilent Technologies, Inc. *User’s Guide for Keysight 33120A Function/Arbitrary Waveform Generator*. 6th ed. Manual. Agilent Technologies, Incorporated. 815 - 14th St. SW, Loveland, Colorado 80537, USA, 2002.

[68] Keithley Instruments, Inc. *Series 2400 SourceMeter® User’s Manual*. Manual. Keithley Instruments, Inc. Cleveland, Ohio, U.S.A., Sept. 2011.

[69] SRS, Inc. *MODEL SR570 Low-Noise Current Preamplifier*. Manual. SRS, Inc. 1290-D Reamwood Avenue, Sunnyvale, California 94089, Aug. 2015.

[70] SRS, Inc. *MODEL SR830 DSP Lock-In Amplifier*. Manual. SRS, Inc. 1290-D Reamwood Avenue, Sunnyvale, California 94089, Oct. 2011.

[71] Teledyne LeCroy, Inc. *HDO6000/HDO6000A High Definition Oscilloscopes Operator’s Manual*. Manual. Teledyne LeCroy, Inc. 2020.

Acknowledgments

I would like to express my heartfelt gratitude to the following individuals and organizations for their invaluable support and contributions throughout the completion of this thesis:

- I am deeply grateful to my thesis supervisors, Tafuri Francesco and Montemurro Domenico, for their unwavering guidance, patience, and mentorship. Their expertise and encouragement were instrumental in shaping this research.

- I extend my thanks to my thesis committee members, for their insightful feedback, constructive criticism, and commitment to ensuring the quality of this work.

- I am indebted to all the participants who generously shared their time and insights for this study. Thanks to Raffella, Davide, Halima, Roberta, Pasquale, Anna, Carlo, Viviana, Luigi and Fabio. Especially to Raffaella and Roberta, your contributions were fundamental to collecting the data necessary for this research, taken with unprecedented seriousness and accuracy. Your patience had no limit.

- To my family, Giovanni, Caterina, Sara, Alessandro, Dalia and Dafne, your unwavering support, love, and understanding have been my pillars of strength throughout this academic journey. Thank you for always believing in me. Especially I acknowledge the financial support provided by my parents , which made it possible for me to carry out this degree. Their investment in my academic pursuits has been invaluable.

- To Maria, In the whirlwind of academic challenges and long hours of research, your presence has been the guiding light that consistently led me back to reality. Your unwavering strength and resilience have inspired me beyond words.

  Amidst the chaos, you've shown me what true determination and perseverance look like. Your unwavering belief in me, even when I doubted myself, has been my motivation.

- My friends, Giovanni, Salvatore, Crescenzo, Giuseppe, Andrea and Lorenzo. I am grateful for your encouragement, understanding, and occasional distractions during the stressful times of thesis writing and during university studies. Your friendship has been a source of motivation.

- Mauro and Luigi, your introduction to power-lifting not only transformed my physical strength but also instilled in me the discipline and determination required to excel in academia. Your unwavering support during a particularly challenging period in my life was a lifeline that I will forever cherish. Beyond our shared passion for power-lifting, our conversations have been a constant source of enlightenment and inspiration. Your unique perspective and depth of knowledge have expanded my horizons and enriched my intellectual growth.

- I would like to extend my heartfelt thanks to two exceptional individuals, Antonio and Francesco. Throughout my degree journey, they have been not only friends but also pillars of support and companions in some of life's most memorable moments. Beyond academics, we've also shared countless moments of camaraderie and laughter. Our sushi outings, in particular, have been a delicious highlight of our friendship, symbolizing the joy and celebration of our shared experiences.

- I would like to thank my colleagues Fabio, Leonardo, Lorenzo and Paolo, at University of Naples Federico II for their camaraderie, stimulating discussions, and shared experiences that enriched my academic life. In particular Fabio, with whom, in addition to having spent countless hours traveling to university, I also prepared 20 exams together.

- I would like to extend my heartfelt appreciation to "Ponys," the extraordinary organization dedicated to outreach and community service. Our journey together has not only been enriching but also profoundly transformative. My personal involvement with "Ponys" has been a privilege and a source of tremendous personal growth. Working alongside such dedicated individuals has shown me the power of collective action and the profound impact it can have on the lives of others.

- I would like to thank Nicola, undisputed head of the teaching secretariat of the physics department. A personality so special that it makes bureaucracy, which in Italy is a burden, a pleasant walk.

- Special thanks go to Blizzard for creating World of Warcraft and Overwatch, with whom I spent unforgettable hours during my degree journey.

- I would like to thank the coffee machine of the geology department, for the great "Ferrarino Ducale" also known as "$\frac{1}{2}$10".

- I would like to thank the wonderful applications created by Microsoft: Paint 3D and Paint

This thesis would not have been possible without the collective support and encouragement of these wonderful people and organization. Thank you for being a part of this journey.

Marcello, October 2023